Neuron
Article

A Cellular Resolution Map of Barrel Cortex Activity during Tactile Behavior

Simon P. Peron,[1] Jeremy Freeman,[1] Vijay Iyer,[1] Caiying Guo,[1] and Karel Svoboda[1,*]
[1]Janelia Research Campus, Howard Hughes Medical Institute, 19700 Helix Drive, Ashburn, VA 20147, USA
*Correspondence: svobodak@janelia.hhmi.org
http://dx.doi.org/10.1016/j.neuron.2015.03.027

SUMMARY

Comprehensive measurement of neural activity remains challenging due to the large numbers of neurons in each brain area. We used volumetric two-photon imaging in mice expressing GCaMP6s and nuclear red fluorescent proteins to sample activity in 75% of superficial barrel cortex neurons across the relevant cortical columns, approximately 12,000 neurons per animal, during performance of a single whisker object localization task. Task-related activity peaked during object palpation. An encoding model related activity to behavioral variables. In the column corresponding to the spared whisker, 300 layer (L) 2/3 pyramidal neurons (17%) each encoded touch and whisker movements. Touch representation declined by half in surrounding columns; whisker movement representation was unchanged. Following the emergence of stereotyped task-related movement, sensory representations showed no measurable plasticity. Touch direction was topographically organized, with distinct organization for passive and active touch. Our work reveals sparse and spatially intermingled representations of multiple tactile features.

INTRODUCTION

Even simple choice behaviors involve large numbers of neurons in multiple brain areas (Guo et al., 2014b; Romo, 2013). Due to technical limitations, neurophysiological recordings typically sample only a small subset of neurons (Stevenson and Kording, 2011), limiting our understanding of neural representations and their relationship to neural circuit structure. Two-photon microscopy (Denk et al., 1994; Svoboda and Yasuda, 2006) has been used to image the activity of populations of individual neurons in anesthetized (Kerr et al., 2005, 2007; Ohki et al., 2006; Ohtsuki et al., 2012; Sato et al., 2007; Stosiek et al., 2003) and behaving (Andermann et al., 2010; Dombeck et al., 2007; Huber et al., 2012; Komiyama et al., 2010) animals. Recent advances in genetically encoded calcium indicators (GECIs) (Chen et al., 2013b; Nagai et al., 2004; Tian et al., 2009) permit sensitive detection of neural activity in individual neurons and tracking of activity in neural populations across days or weeks (Huber et al., 2012; Margolis et al., 2012; Peters et al., 2014). Two-photon microscopy can sample neurons densely, localize them, and measure activity in defined cell types (Chen et al., 2013a; Chen et al., 2013b; Sato and Svoboda, 2010). To date, imaging with cellular resolution in the mammalian brain has been limited to hundreds of neurons in small tissue volumes.

Mice move their whiskers over objects to localize and recognize them (Diamond et al., 2008). The vibrissal primary somatosensory cortex (vS1, or "barrel cortex") contains a somatotopic map of the large facial whiskers (Woolsey and Van der Loos, 1970). Tactile information from individual whiskers is processed in single barrel columns in vS1 (Feldmeyer et al., 2013; Simons, 1978). Each column (diameter, 300 μm) contains approximately 10,000 neurons (Hooks et al., 2011; Lefort et al., 2009). Rodents can localize objects and walls under head-fixed (O'Connor et al., 2010a; Sofroniew et al., 2014) and freely moving (Hutson and Masterton, 1986; Knutsen et al., 2006) conditions using a single whisker. Single barrel columns thus provide a defined target for comprehensive and dense, cellular-resolution imaging.

vS1 comprises distinct layers, with each layer harboring neuron types with distinct inputs and outputs. Input from VPM primarily targets L4, with minor projections to L3, L5B, and L6. Input from POm terminates in L5A and L1 (Lu and Lin, 1993; Petreanu et al., 2009; Wimmer et al., 2010). Other cortical areas send projections to specific laminae in vS1. Vibrissal motor cortex axons terminate in L6 and L1, synapsing onto L2/3, L5, and L6 neurons (Kinnischtzke et al., 2014; Petreanu et al., 2009). Within the cortex, L4 neurons project to L3, and L3 and L5A neurons project to L2 (Feldmeyer, 2012; Staiger et al., 2014). L2 and L3 neurons project to L5 and other parts of the neocortex. L2/3 is therefore a site of integration of ascending sensory input and top-down modulation from higher cortical areas.

vS1 neurons are sensitive to whisker deflections (Ahissar et al., 2001; Armstrong-James et al., 1992; Kerr et al., 2007; Sato et al., 2007; Simons, 1978), with deflection direction mapped topographically in superficial cortical layers (Andermann and Moore, 2006; Kremer et al., 2011). During active behavior, activity in vS1 is modulated by object touch and whisker movement (Crochet et al., 2011; Curtis and Kleinfeld, 2009; de Kock and Sakmann, 2009; Krupa et al., 2004; O'Connor et al., 2010b; Petersen and Crochet, 2013). However, little is known about the prevalence of different sensory representations and their spatial distribution within and across barrel columns.

We used volumetric two-photon laser scanning microscopy, combined with expression of GCaMP6s (Chen et al., 2013b),

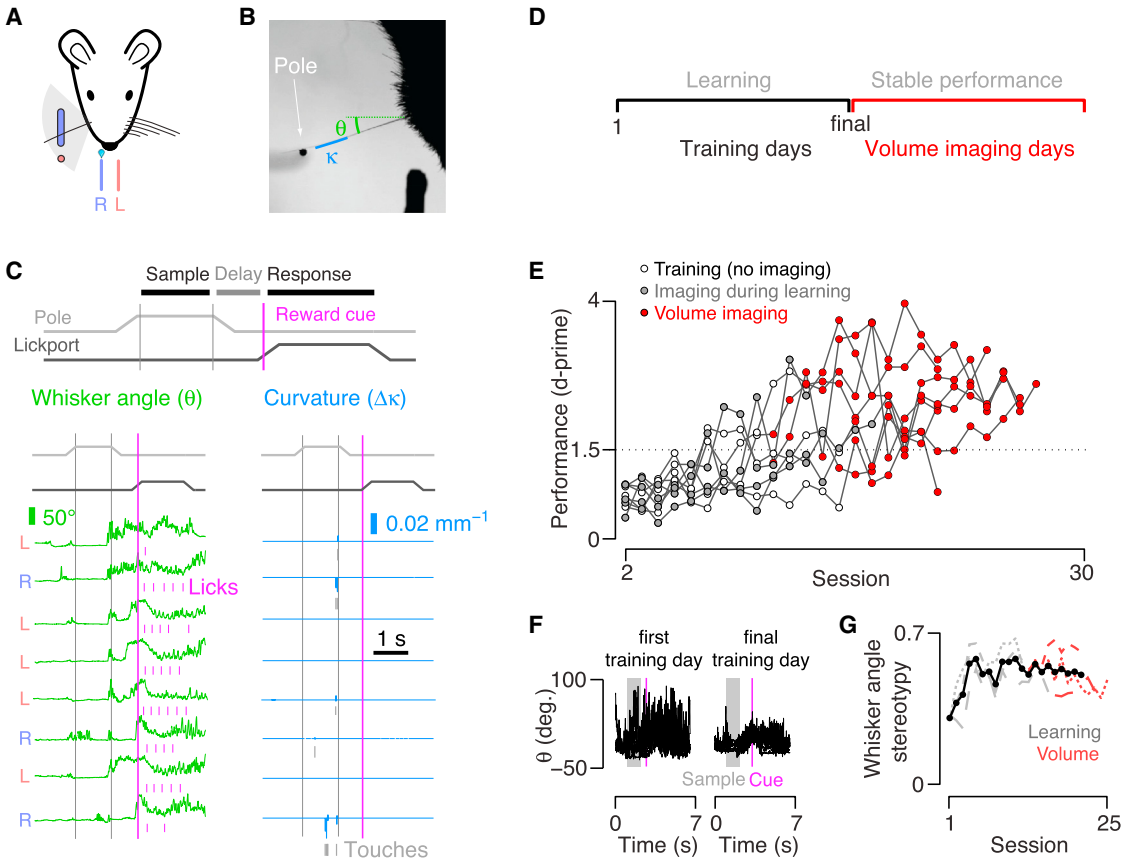

Figure 1. Whisker-Based Object Localization Behavior

(A) Mice were trained to lick the right (blue) lickport if the pole appears in the blue range of positions, or the left (red) lickport if it appears at the red position. Light gray fan, range of whisking.

(B) Single frame from whisker video (500 Hz) with whisker position (θ) and curvature (κ).

(C) Behavioral data for a series of trials. Individual trials consist of a sample epoch, during which the pole is within reach of the whisker (1 to 2 s); a delay epoch (1 s), during which mice have to withhold licking; and a response epoch, triggered by an auditory "reward cue," when mice should signal their behavioral choice. Green, whisker angle (θ, left panel); blue, curvature change (Δκ, right panel); gray ticks, touches.

(D) Experimental timeline.

(E) Performance (d-prime) as a function of training day for individual animals. Dotted line, criterion, d-prime > 1.5. White circle, no imaging; gray circle, imaging during learning; red circle, volume imaging.

(F) Example whisker position trajectory for ten randomly selected trials on first and final training days. Gray, sample epoch; magenta, reward cue.

(G) Whisker angle stereotypy, as quantified by trial-to-mean correlation (see Supplemental Experimental Procedures) for the three mice with the longest period of videography during training. Black, mean; gray, individual animals during learning; red, individual animals during volume imaging.

to measure behavior-related activity in more than 10,000 neurons per mouse in and around the barrel column corresponding to the whisker used by mice to solve a tactile task. This includes the majority of neurons in superficial vS1. Using an encoding model, we quantified the contribution of behavioral variables to the activity of individual vS1 neurons. We thereby constructed a nearly complete cellular resolution map of behavior-related activity for vS1.

RESULTS

Imaging Large Neuronal Populations in Behaving Mice

Head-fixed mice were trained to perform an object localization task with a single whisker. A pole was either presented in a range of proximal positions that predicted a reward in the right lickport (of two) or in a distal position, which predicted reward in the left lickport (Guo et al., 2014a, 2014b) (Figure 1A). Mice had to make a decision about object location and hold this decision in memory during a delay epoch before signaling their decision by licking. We used videography and automated whisker tracking (Figure 1B) to measure whisker movements and tactile input (Figure 1C) (Clack et al., 2012; Pammer et al., 2013). Mice searched for the pole with their whisker, mainly toward the end of the sample epoch (Figure 1C). Whisker position was measured as the azimuthal angle of the spared vibrissa (θ). As a measure of tactile input, we extracted touch-induced changes in whisker curvature (Δκ), which are proportional to the forces acting on mechanoreceptors in the follicle (Birdwell et al., 2007; Pammer et al., 2013).

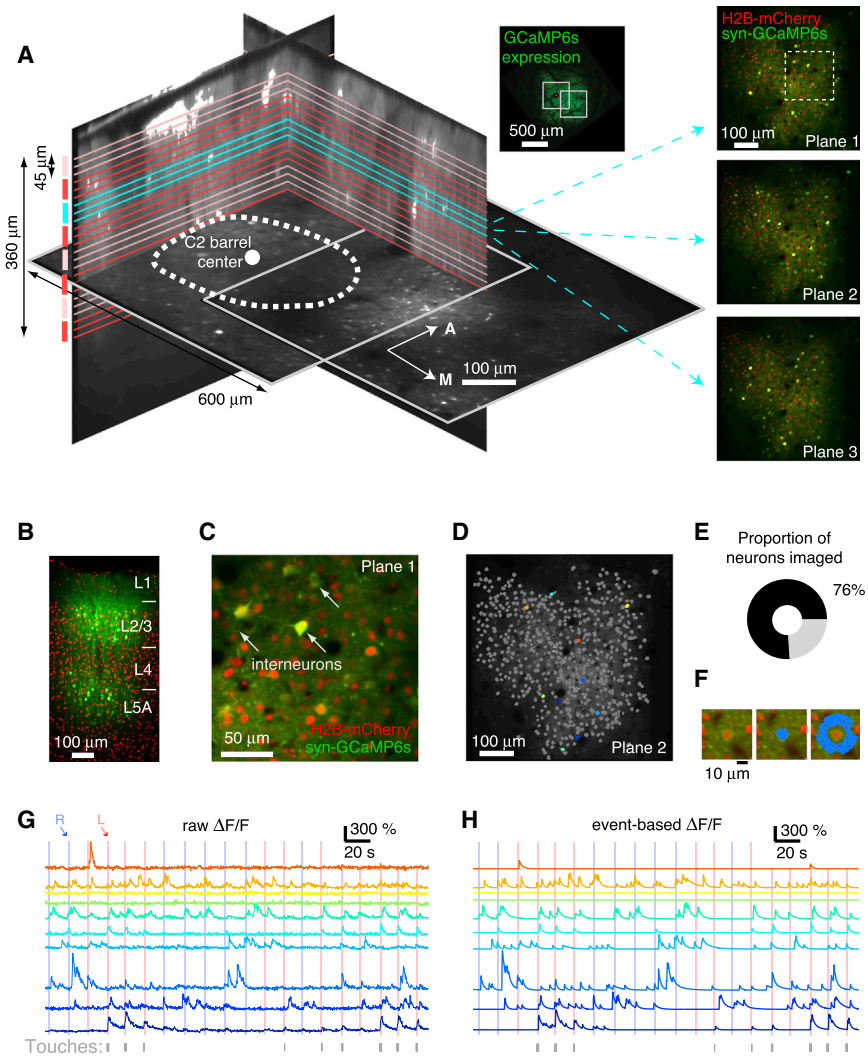

Figure 2. Volume Imaging in Behaving Animals

(A) The basic experiment. Subvolumes consist of three imaging planes (cyan lines) imaged simultaneously (inter-plane distance: 15 µm). Eight subvolumes (red shades, cyan) comprise a volume. Two volumes (gray boxes) were imaged per mouse. Inset, tangential view of the brain (gray, volume boundaries; red dot, center of the principal column). Green fluorescence indicates GCaMP6s expression. Right, three example imaging planes (green, GCaMP6s fluorescence; red, mCherry fluorescence).

(B) Laminar distribution of GCaMP6s expression (green). Red, mCherry fluorescence (*Emx1-Cre* × *Rosa26-LSL-CAG-H2B-mCherry* mouse).

(C) Closer view of plane 1 in (A) (dashed box). Gray arrows, putative GABAergic neurons.

(D) Somatic ROI masks from plane 2 in (A).

(E) Average percentage of excitatory L2/3 neurons imaged (n = 5 volumes).

(F) Neuropil ROI generation. Left to right: raw image (green, GCaMP6s; red, mCherry), neuronal ROI, and neuropil ROI (Figure S3).

(G) Raw ΔF/F traces of neurons colored in (D). Blue and red vertical regions indicate sample epochs for right and left trials, respectively. Gray, touches.

(H) Event-based ΔF/F traces corresponding to (G).

In most cases, imaging began after mice attained stable behavior ("Volume imaging"; Figure 1D; Table S1). A subset of mice was also imaged during training ("Imaging during learning"). Mice reached criterion level performance (d-prime > 1.5, or approximately 70% trials correct; Figure 1E) after 11 ± 4 days (mean ± SD; n = 8 mice) of training. Whisker movements became stereotyped early during training (Figure 1G; Supplemental Experimental Procedures) (Huber et al., 2012), whereas behavioral performance increased more gradually (Figure 1E). Mice performed 245 ± 71 trials per session during imaging. Compared to similar tasks with two pole locations (Guo et al., 2014b), our task elicited larger amplitude whisker movements (approximately 20° versus 55.5° ± 13.3°; mean ± SD; n = 8 mice). A large range of whisking angles and whisker curvatures were sampled during behavior, allowing us to relate neural activity to the dynamics of whiskers.

We performed large-scale calcium imaging in vS1 within the column of the spared whisker (principal column) and its neighbors (Figures 2A and S1). In most experiments (Table S1), mice expressed a red fluorescent protein (mCherry; Shaner et al., 2004) in the nuclei of cortical glutamatergic neurons (*Emx1-Cre* × *Rosa26-LSL-H2B-mCherry*; Figure S2). One mouse expressed mCherry in the nuclei of GABAergic neurons (*Gad2-T2A-NLS-mCherry*). The labeling allowed us to distinguish glutamatergic ("excitatory") and GABAergic neurons. In addition, the red nuclear fluorescence was used to detect neurons in images independent of functional signals. We infected all neurons in and around the principal column with AAV2/1 syn-GCaMP6s, yielding labeled neurons in layers 1, 2, 3, and 5, but not layer 4 (Figure 2B). A cranial window was placed over the infected area (Huber et al., 2012; Trachtenberg et al., 2002).

Following viral injection, mice were water restricted and trained on the pole localization task (Guo et al., 2014a). Two-photon excitation with 1,000 nm light produced emission from both GCaMP6s (green) and the nuclear mCherry (red) (Figures 2A and 2C). Laser scanning in the plane was performed with a custom resonant scanning system (line frequency 16 kHz) (Fan et al., 1999), with axial scanning controlled by a piezo collar. For each trial (approximately 10 s), we imaged subvolumes comprising three planes (600 × 600 μm^2; 512 × 512 pixels) 15 µm apart in depth. Each subvolume was imaged at 7 Hz for 32 ± 7 trials, followed by another subvolume, and so on. Over approximately two behavioral sessions, we visited 16 subvolumes, spanning six to eight barrel columns. Each subvolume was imaged during 4.0 ± 1.2 behavioral sessions.

Regions of interest (ROIs) were drawn in a semi-automated manner around individual somata, aided by the nuclear mCherry fluorescence (Figure 2D; see Experimental Procedures). Our core data set comprised 82,732 excitatory L2/3 neurons, 777 L1 neurons, and 3,806 L2/3 GABAergic neurons (n = 8 mice; Table S1). The mCherry labeling allowed us to quantify the fraction of recorded excitatory L2/3 neurons. Red nuclei were counted in high-resolution stacks of the imaged volumes (Figure S2; see Experimental Procedures). After aligning the imaging planes to these stacks, we estimated the fraction of excitatory neurons for which ROIs had been defined. In L2/3, 76% ± 6% of red nuclei had corresponding ROIs, implying that we had recorded from ~3/4 of the excitatory neurons in L2/3 (Figure 2E). Our count for L2/3 pyramidal neurons per barrel column (1,796 ± 299; n = 5 volumes, see Experimental Procedures) is in agreement with reported neuronal counts for mouse vS1 (Hooks et al., 2011; Lefort et al., 2009). We found 3,806 GABAergic neurons among 86,538 neurons in L2/3 (4.3%). Given that approximately 15% of neurons in L2/3 are GABAergic (Lefort et al., 2009), this implies that we are recording from 1/3 of the GABAergic neurons present in our imaging planes (Experimental Procedures).

Viral transfections produce densely labeled neuropil, consisting of GCaMP6s-expressing axons and dendrites, showing behavior-related activity (Figure S3). Because of the limited resolution of two-photon microscopy in vivo, especially axially (Ji et al., 2012), the neuropil signal bleeds into the somatic signal (Chen et al., 2013b; Ji et al., 2012). We corrected for neuropil contamination by subtracting the local, peri-somatic neuropil signal (Figures 2F and S3; see Experimental Procedures) (Kerlin et al., 2010) and computed ΔF/F for each neuron (Figure 2G). Fluorescence events corresponding to neural activity were extracted using a greedy template-fitting algorithm, similar to the peeling method (Lütcke et al., 2013) but incorporating the variable decay time constants of GCaMP6s (see Experimental Procedures; Figure 2H). Events were then convolved with their respective rise and decay times, to generate a de-noised, event-based ΔF/F trace. All subsequent analyses employed this event-based ΔF/F trace, unless noted.

In deep L3, the cross sections of apical dendrites of L5 neurons appeared as small, high-contrast circles (Figure S4). We verified that ΔF/F in apical dendrites reflected somatic activity by simultaneously imaging apical dendrites in deep L3 and the corresponding somata in L5A. First, manual inspection of 845 events (n = 42 dendrite-soma pairs, n = 3 mice) revealed that 91.0% ± 15.1% of somatic events (mean ± SD) had corresponding dendritic events, and 90.9% ± 12.7% of dendritic events had corresponding somatic events. Second, the correlation between the somatic and dendritic signals was 0.63 ± 0.11 (Pearson's R; $p < 0.001$, n = 42 pairs). This correlation has to be interpreted in the context of the different fluorescence dynamics in the two compartments. Specifically, dendritic responses were larger and briefer compared to somatic transients (Figure S4) (Helmchen et al., 1999; Hill et al., 2013; Svoboda et al., 1997, 1999). We computed the correlation in a model with perfect correspondence between somatic and dendritic events, where the events were convolved with compartment-specific calcium response kernels (to reflect different amplitude and kinetics) and compartment-specific noise was added. The resulting correlation, R = 0.69 ± 0.28 (mean ± SD, correlation $p < 0.001$; n = 42 pairs), was similar to the experimentally measured correlation (Wilcoxon signed rank test, p = 0.063). Thus, activity measured in L5 dendrites measured in L3 reports activity of L5 somata. We imaged a total of 2,469 apical dendrites as a proxy for L5A somatic activity. Based on estimates of neuronal density in L5A (Lefort et al., 2009), we recorded from approximately 10% of these neurons.

Task-Related Activity

Our goal was to understand how the coding of behavioral variables is distributed across neurons in the barrel cortex. The majority of neurons were not silent (event rate > 0.0083 Hz; Figure 3A). The lowest proportion of active neurons was seen in L2/3 excitatory neurons (67% ± 5.4%; n = 8 mice), in quantitative agreement with electrophysiological recordings (O'Connor et al., 2010b).

We examined whether activity was temporally locked to the trial (Figures 4A and 4B; see Experimental Procedures). Overall, 40% of neurons showed task-related activity (Figure 3B). The proportion of task-related neurons was lowest in L2/3 (39% ± 2.9%), intermediate for L5 excitatory neurons (43% ± 4.1%), and high for GABAergic neurons, both in L1 and L2/3 (57% ± 12% and 63% ± 7%, respectively).

The temporal dynamics of L2/3 neurons were diverse. Across the population, activity spanned the behavioral trial (Figure 4C), with a pronounced bias toward the sample epoch during which the animal interacted with the stimulus. In the principal barrel column, activity in the sample epoch was substantially elevated relative to surround columns for all excitatory neuron classes examined (Figure 4D), consistent with somatotopically organized touch input. GABAergic neurons showed distinct dynamics. In addition to a response peak during the sample epoch, GABAergic neurons in L1 and L2/3 were active around the reward cue, which was especially prominent in surround columns (Figure 4D).

Activity in vS1 during the sample epoch is necessary for pole localization (Guo et al., 2014b). The task-related activity observed during the sample epoch may therefore be used by mice to judge object location. To assess the discriminative capacity of individual neurons, we measured how neurons differentiate trial types using receiver-operating characteristic analysis (see Experimental Procedures). Only activity up to the reward cue was used. Among L2/3 excitatory neurons in the principal column, 9.7% ± 8.5% discriminated trial type above chance level (n = 8 mice; Figure 3C). L5 excitatory (17.3% ± 7.1%) and L2/3 GABAergic neurons (20.7% ± 11.5%) performed better. A majority of neuropil ROIs were discriminative (56.1% ± 31.4%). Thus, representation of task-related parameters in L2/3 excitatory neurons of vS1 is sparse (Barth and Poulet, 2012).

Encoding Model of Neural Coding

Vibrissal S1 neurons encode aspects of forces acting on the whisker and whisker movements (Crochet et al., 2011; de Kock and Sakmann, 2009; Fee et al., 1997; O'Connor et al. 2010b, 2013). To investigate which behavioral parameters are

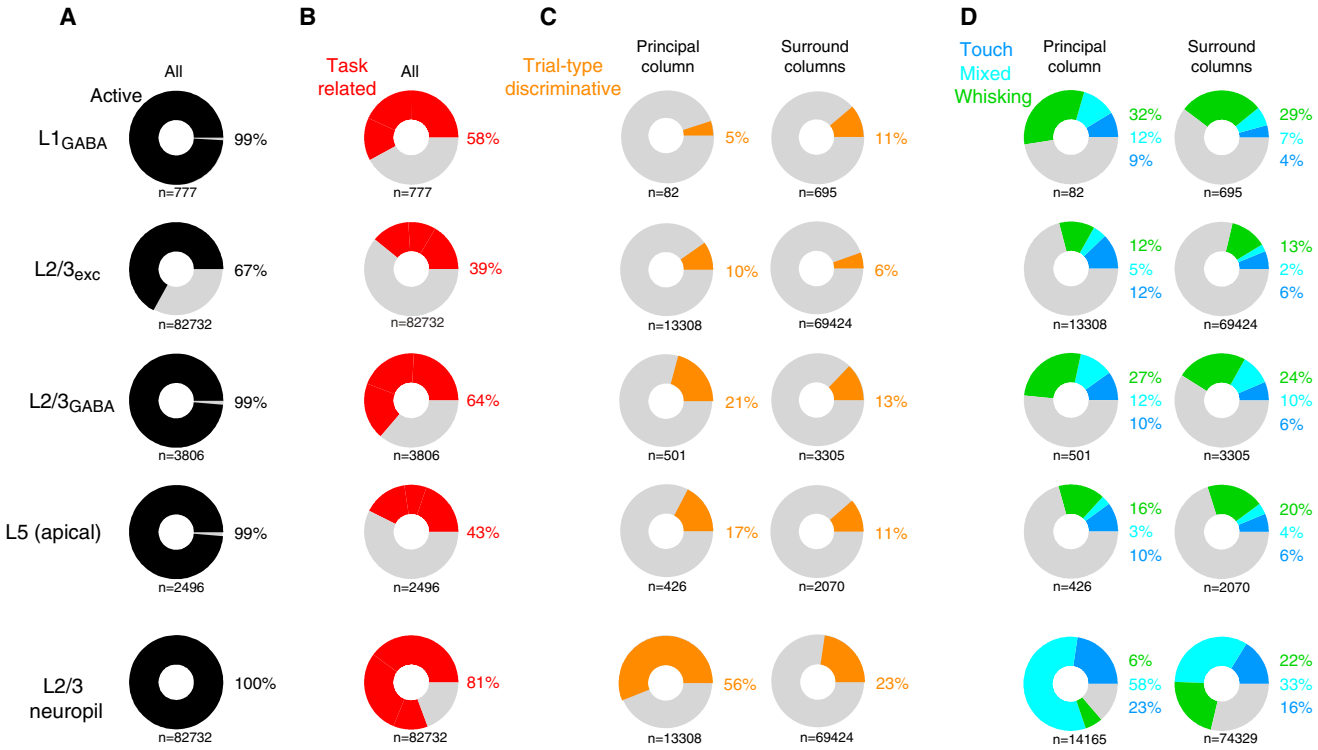

Figure 3. Neuronal Activity and Coding in the Barrel Cortex

(A) Fraction of active ROIs across layers and cell types (event rate > 0.0083 Hz).

(B) Task-related activity fraction by population (Figure 4).

(C) Object location discrimination fraction by population.

(D) Encoding class fraction by population (Figure 5). Mixed neurons represented both touch and whisking.

represented by individual vS1 neurons during active somatosensation, we quantified how whisker movements and touches contribute to neural activity.

The data were fit using a cascaded generalized linear model with input nonlinearities (Ahrens et al., 2008; Paninski et al., 2004). A receptive field, modeled as a piecewise static non-linearity applied to each input variable, describes the relationship of each variable to neural activity. A linear temporal kernel models the temporal dynamics of the neuron, including the time course of calcium transients (Figure 5A). The model was fit to each neuron by maximizing the probability of the response as a function of the behavioral input variables (see Experimental Procedures). The behavioral data consisted of whisker movements or curvature changes collated across multiple sessions (128 ± 30 behavioral trials per neuron; Figure 5B). To quantify model performance, the response predicted by the model for each neuron was compared to the actual response using Pearson's correlation (R_{fit}). If a behavioral variable predicted neuronal ΔF/F with an R_{fit} that exceeded the 95th percentile of shuffled R_{fit}s, the cell was classified as encoding that behavioral variable (Figures 5C–5E; see Experimental Procedures).

Touch and whisking neuron responses were aligned to the first touch and whisking bout (see Supplemental Experimental Procedures) of a trial, respectively (Figure 5F). Layer 2/3 excitatory neurons were equally likely to show representation of whisking and touch within the principal column (17.0% ± 5.2% and 16.8% ± 9.0%, respectively; p = 0.938, Wilcoxon signed rank test, n = 8 mice) (Figure 3D). In surround columns, whisking representation dominated (15.0% ± 3.9% whisking versus 8.9% ± 2.0% touch; p = 0.008). Overall, about a quarter of L2/3 excitatory neurons encoded whisker movement or touch, the lowest proportion observed for any group. Among L2/3 GABAergic neurons as well as L5 excitatory neurons, whisker movements were represented by a larger proportion of neurons compared to touch. The neuropil was dominated by touch, but it also showed detectable encoding of whisker movements in the majority of ROIs.

Imaging during Learning

We examined the dynamics of neural representations during learning of the task (Figure 6A). In four mice (Table S1), we imaged a subset of L2/3 excitatory neurons spanning the principal column and portions of adjacent columns from the onset of training until expert performance was achieved (7, 10, 13, and 17 sessions) (Figures 1D and 1E).

The fraction of touch neurons was constant from the start or middle of training relative to the end of training (Figure 6B) (days 1 and 2 touch fraction: 0.15 ± 0.05, mean ± SD, n = 4 mice, 2 days per mouse; 5 and 4 days before end: 0.14 ± 0.06; final two days: 0.15 ± 0.07; first two versus final two p = 1,

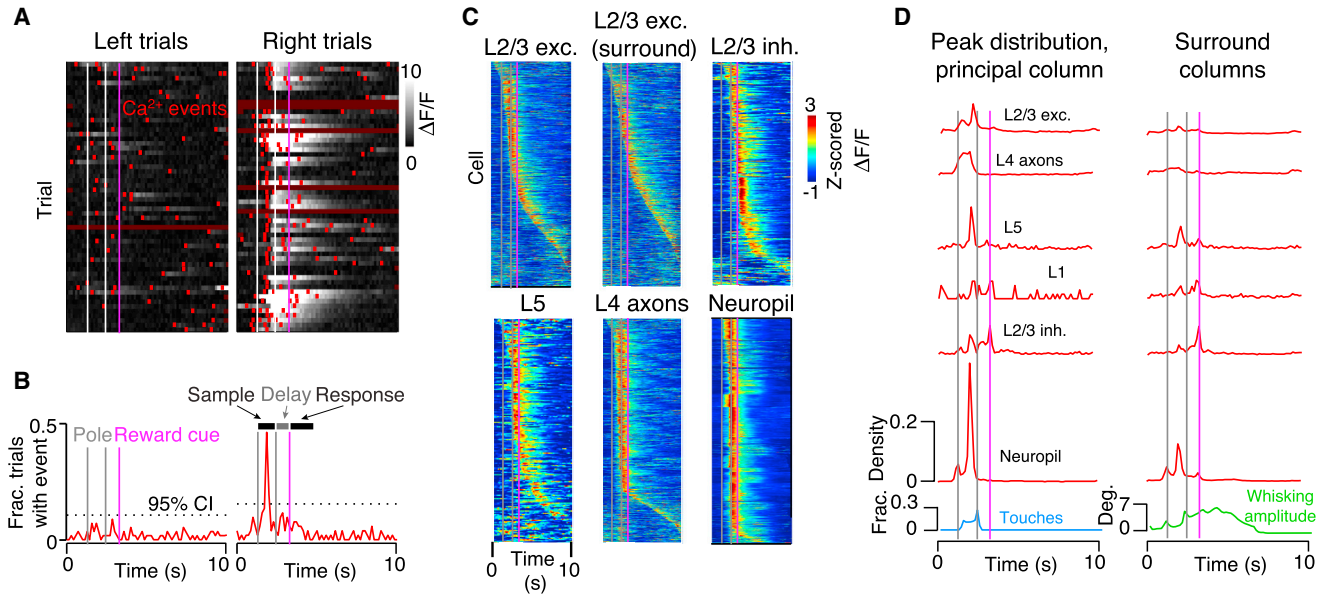

Figure 4. Temporal Distribution of Neural Activity

(A) Measurement of behavior-related activity. Neural activity for right and left trials (only correct trials are shown). Data are trial-aligned. White lines, sample epoch; magenta line, reward cue; red ticks, individual calcium events.

(B) The fraction of trials on which a given trial-aligned time point has an event. Dotted horizontal line, 95% confidence interval of activity peaks based on shuffled data. This neuron shows trial-related activity for right, but not left, trials.

(C) Activity distribution across all ROIs having significant task-related activity. Each line corresponds to a single ROI. The responses are averaged across all trials and z-scored. Neurons are sorted by activity peak time (pooled across animals: n = 3 for L4, n = 8 otherwise). Only ROIs from the principal column were employed, unless noted.

(D) Temporal distribution of activity peaks for different neuronal types (red), aligned to trial time. Green, whisking amplitude; blue, touch fraction (n = 8 mice).

Wilcoxon rank-sum test; middle versus final p = 0.573). The fraction of whisking neurons increased, but only during early training (days 1 and 2 whisking fraction: 0.13 ± 0.04; 5 and 4 days before end: 0.20 ± 0.09; final two days: 0.19 ± 0.05; first versus final p value = 0.010; middle versus final p-value = 0.798). This early increase in the number of whisking neurons parallels early changes in task-related movement (Figures 1F and 1G), suggesting that changing behavior rather than neural plasticity underlies the observed dynamics.

We next looked for functional expansion of the spared whisker representation following trimming, a measure of receptive field plasticity. We compared the fraction of neurons representing touch by the eventual spared whisker inside and outside the principal column after trimming to a single whisker (n = 3 mice, all imaged for at least 10 days after trimming; Figure 6C). We found no change in the ratio of the number of touch neurons (inside-to-outside) following trimming (days 0 and 1: 1.29 ± 0.31; days 4 and 5: 1.55 ± 0.71; days 9 and 10: 1.31 ± 0.39; early versus middle: p = 1; early versus late p = 0.937). Thus, we did not detect enhanced representation of the spared whisker.

Improved task performance during training (Figure 1E) could be a consequence of enhanced representation of object location in vS1 or improved readout by downstream brain areas. We measured discrimination by vS1 neurons during learning. Discrimination by small L2/3 ensembles (ten individually discriminative neurons; Experimental Procedures) exceeded behavioral performance (O'Connor et al., 2010b), even during early training (Figure 6D). Neurometric performance remained flat during learning (first two days: 75% ± 4%, middle two days: 75% ± 5 %, final two days: 78% ± 5 %; first two versus middle two: p = 0.959, first two versus final two: p = 0.721; middle two versus final two: 0.505). In contrast, psychometric performance improved gradually from chance level to criterion levels over the course of training (first two days: 52% ± 2 %; final two days: 66% ± 7 %). This indicates that suitable tactile information is always present in vS1 to perform the task; following learning, mice interpret this information more effectively to gather reward.

We next asked how the representation of touch and whisking evolved at the single neuron level. Individual L2/3 neuron representations stabilized after the first few days of training (Figure 6E): population R_{fit} vectors from early training days were poor predictors of R_{fit} vectors on subsequent days (quantified using Pearson's R), whereas the R_{fit} vectors in later training were better predictors of R_{fit} vectors of subsequent days (Figures 6F and 6G).

Prediction was imperfect across sessions even late in training (i.e., correlation between R_{fit} vectors < 1). This could reflect genuine plasticity in representations or lack of sensitivity when comparing encoding model fits across days. To disambiguate these possibilities, we computed a distribution of correlation values from data without plasticity. Each session was partitioned trial-wise into two equal-length, temporally interdigitated "pseudo sessions." The encoding model was fit to each "pseudo session" independently, and the correlation between

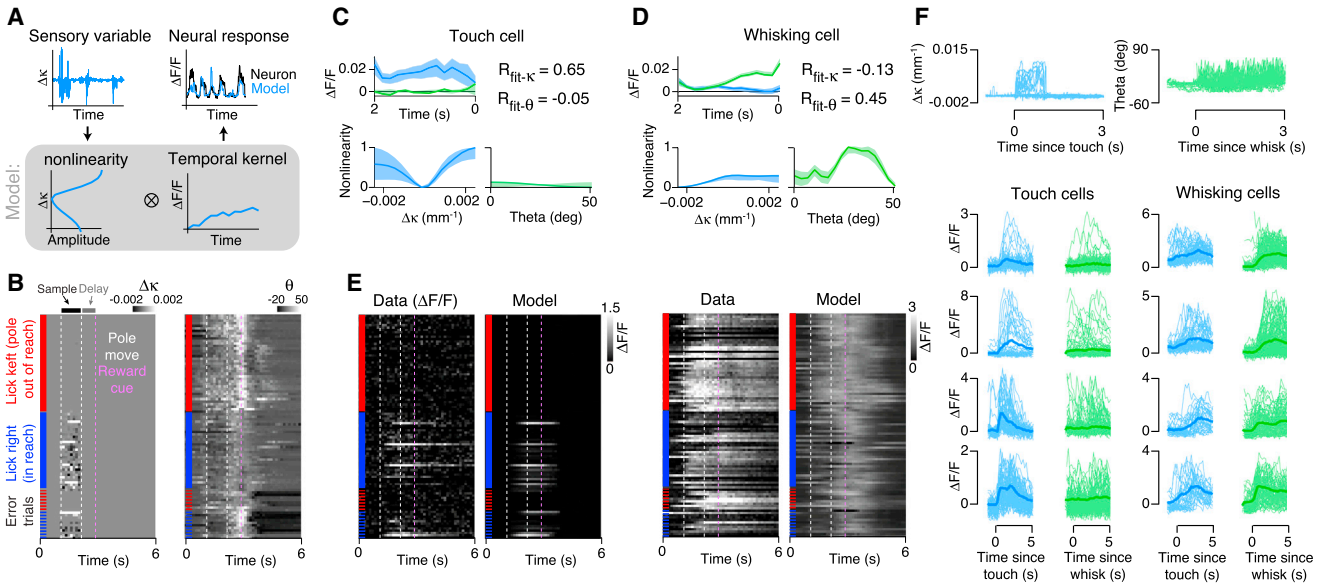

Figure 5. Encoding Model and Neuronal Classification

(A) The encoding model predicts neuronal ΔF/F (top-right, blue trace) from whisker dynamics (top-left; $\Delta\kappa$). The model consists of a nonlinearity, or receptive field (bottom-left), acting on the behavioral variable domain. This is convolved with a temporal kernel (bottom-right), acting on the time domain. The predicted ΔF/F trace (blue) is compared to actual ΔF/F (black) using Pearson's correlation to compute R_{fit} (top-right).

(B) Example behavioral variables used to fit the model for one subvolume. Curvature change ($\Delta\kappa$; left) was zero for non-touch periods. Vertical white dashed lines, sample epoch; magenta lines, reward cue. Blue vertical lines, right trials; red, left trials; stippled red and blue, error trials.

(C) Fit for an example cell (corresponding to behavioral data shown in (B). Top, temporal kernels; bottom, receptive field nonlinearities (green, whisker angle; blue, curvature change; mean ± bootstrap 2.5 and 97.5 percentiles). Though the model produced a receptive field for θ, when the magnitude of the temporal kernel is near 0, as it is here, it implies that the kernel is not informative. This is illustrated by scaling the amplitude of each nonlinearity by the norm of the corresponding temporal kernel.

(D) Same as (C), but for a whisking neuron.

(E) Raw ΔF/F (left) and model-predicted ΔF/F (right) for the two cells in (C) and (D).

(F) Example neural responses aligned to behavior. Top traces, whisker curvature aligned to first touch (blue, left) and whisker angle aligned to first whisking bout (green, right; see Supplemental Experimental Procedures). Remaining traces, ΔF/F aligned to the first touch (blue) or first whisking bout (green) of a trial for example touch (left) and whisking (right) neurons. Light color, individual trials; dark color, mean.

the two resulting R_{fit} vectors was measured. By repeating this 25 times per session, a distribution of intra-day correlation values was obtained. For a given imaging day, subsequent days were considered significantly distinct if the correlation of the R_{fit} vectors fell below the 5th percentile of intra-day correlations for that day.

Touch representations of individual neurons stabilized during training (Figure 6H). Relative to the first day of imaging, 77 % ± 26% (n = 4 mice) of subsequent days were different, whereas 5 days prior to the final training day, only 17% ± 33 % of subsequent days were different. Whisking representations also stabilized. Relative to the first day, 60% ± 43 % of subsequent days were different, falling to 33% ± 36 % 5 days before the end of training.

Our data show that encoding as well as discriminative performance stabilizes after the first few days of training, both at the level of single neurons and populations. This justifies sampling across behavioral sessions to characterize large numbers of vS1 neurons in well-trained mice. The time course of stabilization mirrors the time course of the emergence of motor stereotypy (Figures 1F and 1G), rather than improvement of behavioral performance (Figure 1E).

Spatial Organization of Sensory Coding

We next investigated how the encoding of behavioral variables is organized spatially. Among L2/3 pyramidal neurons, touch and whisking cells were intermingled in a salt and pepper manner within the principal barrel column and also in the surrounding columns (Figures 7A and 7B). The proportion of L2/3 excitatory neurons encoding touch declined by half when moving from the principal column to the surround columns (Figures 7B and 7C; p = 0.008, Wilcoxon signed rank test, n = 8 mice). A similar spatial profile was observed in L1 (p = 0.031). In contrast, touch-encoding L5 neurons (p = 0.383) and L2/3 GABAergic neurons (p = 0.578) were equally likely in the center and surround columns (Figure 3D). Touch thus activates L2/3 GABAergic neurons over multiple columns, producing an inhibitory surround in L2/3 (Derdikman et al., 2003). Representation of whisking was uniform across neurons inside and outside the principal column. Thus, touch neurons were primarily confined to the principal column, whereas whisking neurons were distributed uniformly.

The L2/3 neuropil signal had different dynamics and structure from L2/3 somata (Figures 4C, 4D, and S3). The neuropil signal was temporally more concentrated in the sample epoch and spatially more concentrated in the principal column. This

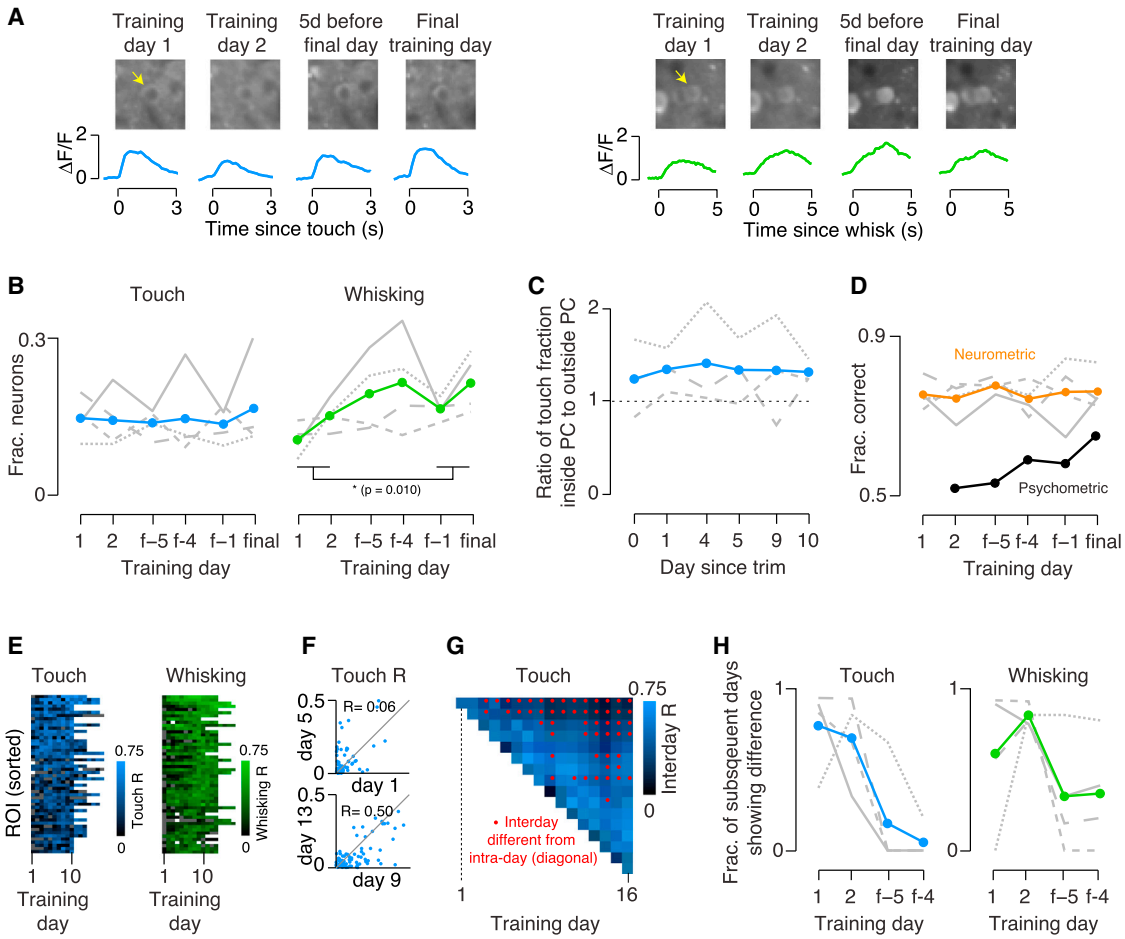

Figure 6. Dynamics during Learning

(A) Example neurons imaged during learning of the object localization task (before volume imaging). Left, touch cell; right, whisking cell.

(B) Fraction of L2/3 excitatory neurons classified as touch or whisking during learning. Mean touch, blue; mean whisking, green; gray lines, individual animals (n = 4).

(C) Ratio of the fraction of neurons representing touch inside the principal column to fraction representing touch outside the principal column with respect to day following single whisker trimming (day 0: day of trimming). Mean is indicated in blue; gray lines, individual animals (n = 3).

(D) Neurometric and psychometric performance over the course of learning. Orange line, task performance of the best ten neuron ensemble; gray lines, individual animals' (n = 4) best ensemble performance; black, cross-animal psychometric performance (the first day of training consisted of a simplified form of the task where the performance metric did not apply and was thus excluded).

(E) R_{fit} of top 50 touch (blue) and whisking (green) neurons over the course of learning, across animals (n = 4). Grey, days where the neuron did not meet the $p < 0.01$ criterion to be counted as a neuron of that category (see Experimental Procedures); white, missing data. Trace length identifies source animal (training length was unique).

(F) Example relationship between the R_{fit} for touch neurons across days. Top panel, the relationship between the first and 5th day; bottom panel, 9th and 13th days.

(G) Example animal's correlation of touch R_{fit} vectors from one day with another (i.e., the R values from [F] for all day-pairs). The diagonal elements show the median correlation of 25 pairs of intra-day R_{fit} vectors (see Results). Red dots, days for which the inter-day correlation fell below the 5th percentile of the intra-day correlation values for the first day of that row.

(H) Fraction of days after the specified day for which the inter-day R_{fit} correlation fell below the 5th percentile of intra-day R_{fit} correlations (red dots in [G]). Blue, touch; green, whisking; gray, individual animals (n = 4).

suggests that it mostly reflects active touch. The neuropil signal did not directly reflect activity in L4 axons, as suggested previously (Kerr et al., 2005), because L4 neurons were not expressing GCaMP6 infection in our preparation. We measured L4 axon activity in a separate set of mice (Figure S5). The spatial distribution of neuropil activity most closely resembled L4 activity. Specifically, the correlation between L4 axon and L2/3 neuropil touch maps was highest of the three possible pairings (L4-neuropil Pearson's R: 0.60; L4-L2/3 somata: 0.41; L2/3 somata-neuropil: 0.36). Temporally, L4 axons and L2/3 neuropil both had a large fraction of activity confined to the sample epoch (Figures 4C and 4D). This suggests that the neuropil corresponds to postsynaptic calcium dynamics in L2/3 neuron dendrites, independent of somatic spikes. Consistent with this interpretation,

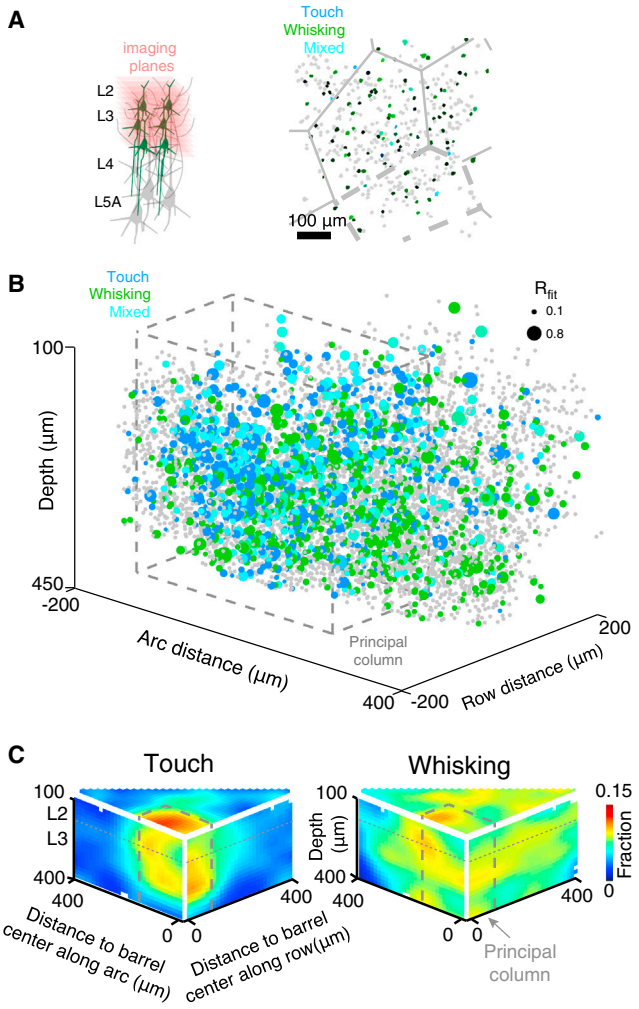

Figure 7. Spatial Distribution of Representations in L2/3

(A) Example imaging plane with somatic ROIs. Blue, touch neurons; green, whisking neurons; cyan, mixed; gray, unclassified. Intensity is proportional to R_{fit}. Thick dashed line, outline of the principal column; thin lines, surround columns.

(B) 3D distribution of response types in one mouse. Blue, touch neurons; green, whisking neurons; cyan, mixed; gray, unclassified; gray dashed line, outline of principal column. Radius indicates R_{fit}.

(C) Map of touch and whisking excitatory neurons across L2/3 (pooled across eight mice). Color represents the fraction of neurons in a given voxel classified as either touch or whisking. Location is in terms of distance from the center of the spared whisker column (dashed line). The maps on top represent the row-arc plane, averaging cell fractions through depth. The arc-depth (left) and row-depth (right) maps average cell fractions across a half-barrel width in the plane-orthogonal direction.

all L2/3 neurons show strong subthreshold responses to touch (Crochet et al., 2011).

We next examined the spatial organization of encoded variables at the fine scale. We found no difference when comparing the distribution of pairwise distances among neurons of a category (touch, whisking, and mixed) to the pairwise distance distribution among all neurons (Figure S6). Thus, different representations were randomly intermixed in L2/3 within a column, but the touch representation showed the expected somatotopic organization on the scale of multiple columns (Kerr et al., 2007; Sato et al., 2007) (Figure 7B).

Directional Tuning in vS1

Directional tuning maps have been observed in rat vS1 (Kremer et al., 2011; Andermann and Moore, 2006). Our encoding model yields a description of how response amplitude varies as a function of whisker curvature (Figures 5A–5D). Because the sign of curvature is different for protraction and retraction touches (negative and positive, respectively), the receptive fields reflect direction preference, allowing us to examine the topography of directional tuning in vS1.

The majority of L2/3 touch neurons were directionally tuned (Figures 8A and 8B), with an approximately equal number of neurons preferring protraction and retraction. Directional tuning was typically strong, with neurons either responding almost exclusively to protraction (directionality index [DI] = 1) or retraction (DI = −1) touches. Relatively few neurons showed an intermediate level of tuning. To assess stability of directional tuning over time, we measured the average pairwise root mean square (RMS) difference among touch receptive fields in the animals imaged during training (n = 4 mice). The difference between touch receptive fields among days (grand mean of RMS difference: 0.273; n = 118 neurons) was below the 5th percentile of the shuffled distribution (0.425; shuffling by neuron identity) for 97.8% of the neurons examined (Figure S4). Thus, L2/3 directional tuning was stable over the course of learning.

Consistent with observations in anesthetized rats (Andermann and Moore, 2006; Kremer et al., 2011), neurons sensitive to protraction touch were more abundant in and near the barrel column of the whisker anterior to the spared one, with retraction-sensitive neurons more abundant in and near the column of the whisker posterior to the spared one (Figures 8C–8E). This trend in direction selectivity within a barrel row (Figure 8E) could be a consequence of neurons becoming more biased (increasing DI magnitude) with distance from the principal column, or it could reflect changes in relative fractions of comparably biased neurons (constant DI magnitude). DI magnitudes inside and outside the principal column were similar (p = 0.333, Wilcoxon rank-sum test), implying that the spatial trend reflects a change in overall directional preference of neurons with similar DI magnitude.

Prior examination of directional tuning using extracellular recordings failed to reveal topographic organization in L4 (Andermann and Moore, 2006). In contrast, we observed a directional map, similar to that observed in L2/3 excitatory neurons, in the activity of both L4 axons and the L2/3 neuropil (Figure 8E). Thus, at least in mice, the directional topography of L2/3 is likely inherited from L4.

Previous work in anesthetized rats showed that forward whisker deflection produced stronger responses in the column of the whisker immediately anterior to that of the deflected one (Andermann and Moore, 2006; Kremer et al., 2011). Active touches during protraction (whisker movement in the anterior direction) produce negative curvature changes, whereas passive whisker deflection in the anterior direction produces positive curvature changes. Despite this difference in curvature sign,

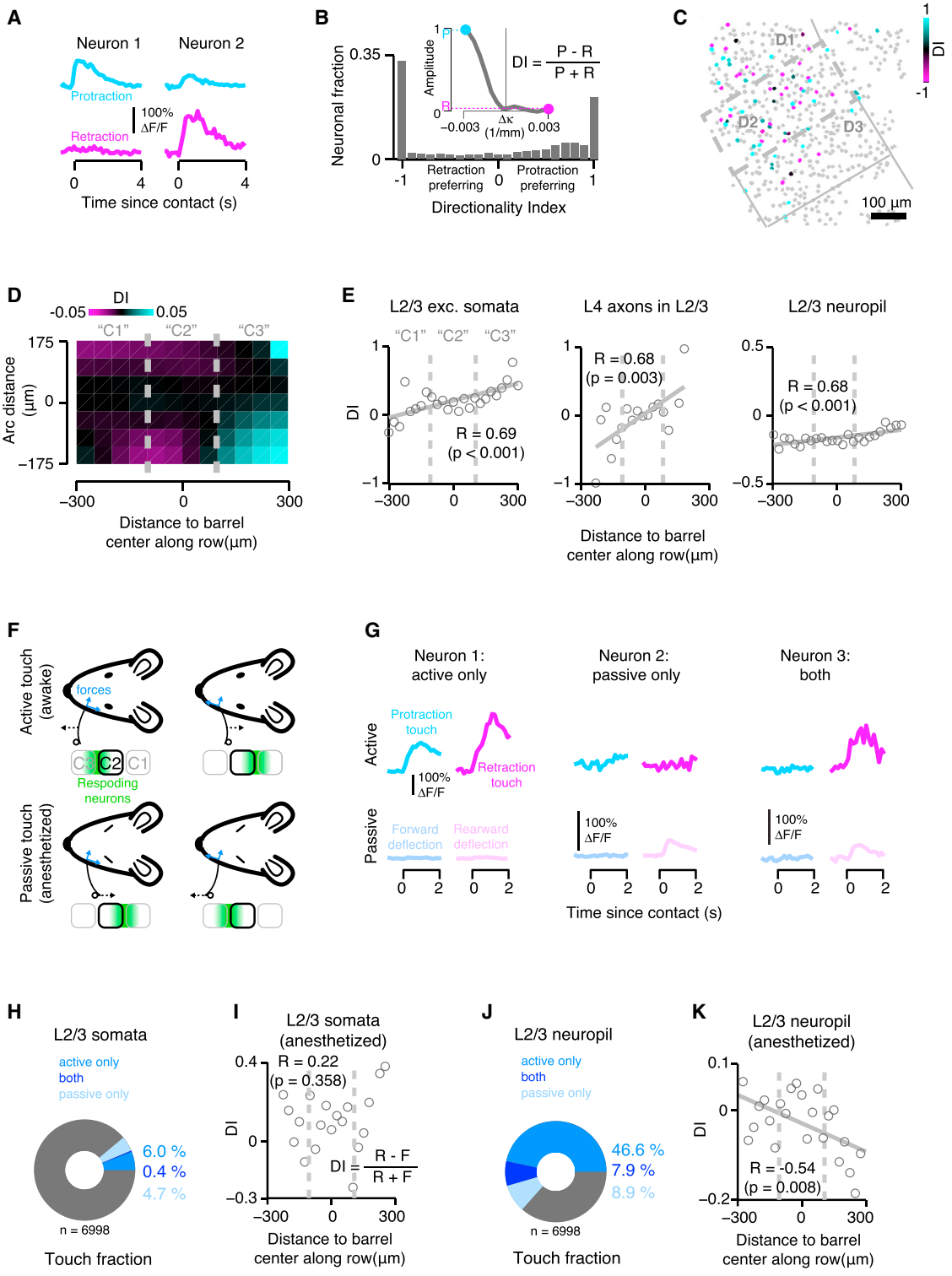

Figure 8. Directional Selectivity Maps in Response to Active and Passive Touch

(A) Two example direction selective touch neurons.

(B) Distribution of DIs (inset) across touch neurons. Positive DI, protraction preferring; negative DI, retraction preferring ($\Delta\kappa < 0$ corresponds to protraction; see Supplemental Experimental Procedures).

(C) Spatial distribution of directional selectivity in an example plane. Color indicates DI for touch neurons. Grey, unclassified. Thick dashed line, outline of the principal column; thin lines, surround columns.

(legend continued on next page)

both cases evoke the most response among neurons in and near the column of the whisker anterior to the spared one (Figure 8F). Since the change in curvature is proportional to the lateral force exerted on the whisker, this implies that the somatotopy in active and passive touch is reversed in terms of lateral forces.

To explore this discrepancy, we compared neural responses to passive touch in anesthetized mice and during active tactile behavior (n = 3 additional mice). In anesthetized mice, whiskers were stimulated with a pole mounted on a piezo (see Supplemental Experimental Procedures). We found that most neurons responded to touch in only one or the other condition, and rarely both. Surprisingly, only 8% of neurons showing touch responses under anesthesia showed touch responses during behavior, with 6.5% expected by chance (Figures 8G and 8H). Therefore, different neurons encode passive whisker deflection and touch during active behavior. Furthermore, in contrast to the topography observed in anesthetized rats, we did not detect topography in directional tuning for neurons in anesthetized mice (Figure 8I).

The neuropil signal was still direction selective under anesthesia (Figure 8J). Moreover, the topography of neuropil directionality under anesthesia was consistent with that observed in anesthetized rats (Kremer et al., 2011): forward deflection elicited responses in and near the column of the whisker immediately anterior to the one deflected (Figure 8K). Thus, both individual neuron touch sensitivity and the overall organization of the directional map differed between actively sensing and anesthetized mice.

DISCUSSION

Even the sensory cortex corresponding to one modality, such as vS1, contains approximately 400,000 neurons spanning 3 mm^3 of brain tissue (Hooks et al., 2011). This large number present a sampling problem for comprehensive measurement of neural activity. To begin to overcome this challenge, we employed single whisker behaviors that depend on activity in the spared barrel column (Guo et al., 2014b; Hutson and Masterton, 1986; O'Connor et al., 2013; Shih et al., 2013). The superficial layers of a single barrel column contain approximately 2,000 neurons (Lefort et al., 2009), providing a tractable target for comprehensive imaging.

We sampled activity in 10,000–20,000 neurons per mouse, including the majority of L1–3 neurons in the principal and neighboring columns during tactile behavior. Nearly half of the neurons showed task-related activity. Here we only analyzed increases in fluorescence. Task-related decreases in fluorescence, consistent with reduced activity, were also observed, but they were slow and weak and not analyzed further. Our estimate of the fraction of silent neurons was in agreement with measurements based on unbiased electrophysiology (O'Connor et al., 2010b).

In the principal column, 12% of L2/3 neurons reported touch, 12% reported whisker movements, and 5% reported both. Representations of whisker movements were distributed uniformly across multiple barrel columns, whereas representation of touch was concentrated in the spared column. We did not observe functional clustering on local scales: neighboring neurons were no more likely to be part of the same representation than expected by chance. Representations of different variables are therefore intermingled in L2/3.

We sampled about 1,200 neurons at 7 Hz. This rate is constrained by the need to sample serially, limited dynamic range of the protein calcium indicator, attenuation of light in tissue, and raster scanning, which makes non-optimal use of imaging time. Our finding of strong and correlated neuropil signals suggest that current methods for parallel sampling, such as light-field microscopy (Prevedel et al., 2014) and light-sheet microscopy (Holekamp et al., 2008), may be inadequate for isolating signals from single neurons in scattering tissue.

Relating neural activity to behavioral variables poses conceptual and computational challenges. Direct comparisons between sensory variables and calcium activity using methods such as correlation fail to incorporate the nonlinear aspects of neuronal tuning and the kinetics of calcium. Moreover, correlation-based methods are difficult to interpret when comparing coding of variables with distinct temporal structure. In our case, whisker angle is temporally dense, whereas touch is temporally sparse, and both often show a nonlinear relationship between the stimulus variable and activity. Pearson's correlation will thus misestimate the relative and absolute encoding of both of these variables. In contrast, encoding models that predict calcium activity explicitly enable principled comparisons between the strengths of coding for touch, whisker movements, and other

(D) Distribution of directional selectivity for excitatory L2/3 excitatory neurons across animals (n = 7). Magenta, retraction preference (DI < 0); cyan, protraction preference (DI > 0). Here, it is assumed that the principal column was C2; in that case, the C1 and C3 columns would be where indicated (gray lines, barrel border). DI was averaged using 50 μm bins.

(E) Directional selectivity along a whisker row for L2/3 excitatory neurons, L4 axons in L2/3, and L2/3 neuropil. DI was averaged using 45 μm bins along the row axis. Positive row axis values correspond to moving toward columns of whiskers anterior to the spared whisker (principal column, gray dotted line; columns labeled for case where PC was C2). Solid gray line, linear fit to points; Pearson correlation coefficient indicated along with p value.

(F) Directional preference map and its relationship to contact forces. In the active touch condition (top), protraction/retraction contacts elicit rearward/forward lateral forces along with a radial force (blue) at the follicle. Responding neurons (green) are predominantly confined to the segment of the barrel close to the whisker immediately anterior/posterior to the one contacted. Under anesthesia, forward/rearward passive deflection produces a spatial distribution of responding neurons similar to protraction/retraction contacts during active touch, but with opposite lateral forces.

(G) Example responses among three neurons for the active, awake (top) and passive, and anesthetized (bottom) conditions. Cyan, protraction touch; magenta, retraction touch; light cyan, forward anesthetized deflection; light magenta, rearward anesthetized deflection.

(H) Fraction of neurons showing touch responses under active (blue) and passive conditions (light blue); dark blue, overlap (n = 3 mice).

(I) Directional selectivity within a whisker row for L2/3 excitatory neurons under anesthesia, as in (E).

(J) Fraction of neuropil ROIs showing touch responses, as in (H).

(K) Directional selectivity among neuropil ROIs in anesthetized mice, as in (E).

behavioral variables (Ahrens et al., 2008; Huber et al., 2012; Miri et al., 2011). Applying a correlation-based approach to our data set classifies a larger proportion of neurons as touch, likely explaining the discrepancy with other imaging studies in the barrel cortex (Chen et al., 2013a).

We employed a probabilistic encoding model to relate neural activity and behavior (Ahrens et al., 2008; Pillow et al., 2008) by explicitly modeling calcium kinetics and nonlinear receptive field shape. In contrast to other algorithms, such as random forests (Huber et al., 2012), this approach is computationally efficient and yields transfer functions that are interpretable as receptive fields (Ahrens et al., 2008) (Figure 5). The computational efficiency of our approach allowed us to run numerous iterations of the model and perform rigorous statistical testing. In addition to more accurate classification, the model produced interpretable receptive fields for whisker curvature, allowing us to examine the topography of directional selectivity.

We related neural activity to the angle and curvature of the spared whisker. These parameters describe the motion of the whisker and the stresses at the follicle where mechanosensation takes place (Birdwell et al., 2007; Pammer et al., 2013; Quist and Hartmann, 2012). Though we did not track torsion about the whisker axis, this should have little impact on neuronal classification because torsion is tightly coupled to whisker angle (Knutsen et al., 2008). Our encoding model produced meaningful $\Delta\kappa$ kernels, but not whisker angle kernels (Figure 5C). Touch neurons with an angular preference should have produced a discernible peak in the whisker angle kernel. This implies that we did not detect tuning to position-at-touch. The encoding model captures nonlinear activity-variable relationships, as demonstrated by the curvature kernels (Figures 5C and S7). It does not capture non-stationary activity relationships, such as adaptation during repeated touches. Moreover, our choice of behavior limits the stimulus space that was probed. For example, we did not explore vS1 responses to slip events typically encountered during exploration of textures (Chen et al., 2013a; Hires et al., 2013; Jadhav et al., 2009; von Heimendahl et al., 2007). It is likely that additional representations of tactile information will be revealed in other behavioral conditions and with the aid of more sensitive encoding models.

Topographic organization of direction selectivity has been reported in both cortex (Andermann and Moore, 2006; Kremer et al., 2011) and thalamus (Timofeeva et al., 2003) of anesthetized rats. We detected directional topography in actively sensing mice. In passively stimulated anesthetized mice, we observed directional topography in the neuropil of anesthetized mice, but not at the level of neurons, suggesting that topography is present but very weak. Passive forward deflection of the whisker produces lateral forces opposite in sign to those experienced upon object contact during forward whisker movement (Birdwell et al., 2007; Hires et al., 2013). Thus, the anesthetized passive deflection tuning maps exhibit opposite organization in terms of lateral force from the map observed in actively sensing mice. Further investigation will be necessary to elucidate the origin of this discrepancy.

A major advantage of imaging is the ability to track activity over multiple days. We find the L2/3 population to be stable in terms of the fraction of neurons participating in the touch representation (Figure 6). Whisking neuron fraction stabilized after the first few days of training, as did the distribution of touch and whisking encoding strength. This time course was consistent with the emergence of motor stereotypy; behavioral performance continued to improve after neural representations and motor stereotypy stabilized (Figures 1E and 1G). Because encoding classification as well as neurometric performance can change in response to the changes in motor strategy, it is possible that these early dynamics are merely a reflection of changing behavior and do not reflect neural plasticity. Although our data are thus ambiguous regarding the nature of early learning, we do find stability in representations during later learning. Such stability contrasts with motor cortex, where representations are more dynamic (Huber et al., 2012; Masamizu et al., 2014; Peters et al., 2014). We neither observed the expansion of the representation of the spared whisker observed in some trimming studies (Margolis et al., 2012) nor observed the spared whisker contraction reported in animals exposed to enriched environments (Polley et al., 2004). The failure to observe map expansion may reflect lack of sensitivity in our imaging, or it could be a consequence of our measuring expansion in behaving rather than anesthetized animals.

EXPERIMENTAL PROCEDURES

Transgenic Mice

The majority of mice in this study expressed mCherry in the nuclei of excitatory neurons. A custom reporter mouse (*Rosa26-LSL-H2B-mCherry*, JAX 023139; Figure S2) was crossed with *Emx1-IRES-Cre* (JAX 005628) (Gorski et al., 2002). The *Rosa26-LSL-H2B-mCherry* mouse was generated by targeted insertion of a construct containing the CAG promoter followed by a floxed-Stop cassette-controlled nuclear red fluorescent protein (Madisen et al., 2012) at the *Rosa26* locus. The woodchuck hepatitis virus posttranscriptional regulatory element (WPRE) was used to enhance mRNA transcript stability. We chose mCherry as the fluorescent protein because its fluorescence emission spectrum does not overlap with GCaMP6 (Shaner et al., 2004). The nucleus was targeted by fusing mCherry to the histone protein H2B. Using the pair of PhiC31 recognition sites, *AttB*/*AttP*, the *PGK-Neo* marker can be deleted from the reporter lines in mice. Removal of the Stop cassette by Cre expression produces strong, red nuclear fluorescence in Cre-expressing cells.

We also generated a *Gad2-T2A-NLS-mCherry* mouse (JAX 023140; Figure S2), which expresses mCherry in the nuclei of GABAergic interneurons. *T2A-NLS-mCherry* was inserted in-frame after the last codon of the *Gad2* gene. Insertion was verified using a *frt-Neo-frt* cassette. This was removed by crossing the chimeras with *R26-FLP* females (JAX 003946). Nuclear targeting was achieved using by fusing mCherry to a nuclear localization signal (NLS) sequence.

Surgeries

AAV2/1 syn-GCaMP6s (Penn Vector Core #Av-1-PV2824) was injected into vS1 of anesthetized mice, and a cranial window was placed over the injection site. All animal procedures were in compliance with protocols approved by the Janelia Farm Research Campus Institutional Animal Care and Use Committee.

Behavioral Training

Animals were water restricted and trained on a pole localization task, which required them to select one of two lickports based on whether the pole was in a proximal or distal location (Guo et al., 2014b). Whisker movement was recorded using high-speed videography. Whiskers were stimulated during anesthesia using a piezo-driven stimulator.

Two Photon Imaging

Calcium imaging was performed using a custom two-photon microscope (http://openwiki.janelia.org/wiki/display/shareddesigns/MIMMS). Images were acquired using a 16× 0.8 NA objective (Nikon) and GaAsP PMTs (Hamamatsu). Green (GCaMP; BG22, Chroma) and red (mCherry; 675/70 emission filter, Chroma) fluorescence channels were collected simultaneously. Horizontal scanning was accomplished using a resonant galvanometer (Thorlabs; 16 kHz line rate, bidirectional). Axial motion was controlled by a piezo collar (Physik Instrumente). Powers at the sample ranged from 30 mW in L1 to 300 mW in L5. Exponential power modulation (λ = 250 μm) was employed during piezo scanning. Four 600 × 600 μm (512 × 512 pixels) imaging planes were acquired at 7 Hz each across depth. The system was controlled using ScanImage (http://scanimage.org) (Pologruto et al., 2003).

The three imaging planes were either 15 μm (volumetric and L4 axon data) or 120 μm (imaging during learning and L5-L3 simultaneous imaging data) apart; the fourth fly-back frame was discarded. Each set of three planes constituted a subvolume (Figure 2A). Learning data tracked a single subvolume over multiple sessions. For volume imaging, each subvolume was imaged for 4.0 sessions (mean; range, 1–8), with data pooled across sessions. Eight subvolumes comprised a single volume, and two volumes were imaged per animal. These spanned 360 μm in depth (L1-L3). For L4 axon imaging, six subvolumes in a single volume over the spared whisker barrel were imaged (L2-L3; spanning 270 μm in depth). For simultaneous imaging of L5 somata and deep L3 apical dendrites, the top and bottom planes of the subvolume were employed, for an inter-plane distance of approximately 240 μm.

After the first imaging session, average images of each imaged plane were generated. At the beginning of all subsequent imaging sessions, these four images (three imaged planes and one fly-back plane) were employed as references while imaging. Positional adjustments were made to ensure that the same neurons were imaged over the course of the session (Huber et al., 2012). On the middle imaging day, a high-resolution stack (1 μm spacing) was acquired, and all imaging planes were aligned to this stack to establish the relative positions of neurons. In *Emx1-Cre* × *LSL-H2B-mCherry* animals, the locations of individual neuronal nuclei were determined using the red channel of this reference stack (Figure S2) and a 3D Gaussian mixture model. Briefly, the model looked for spheres whose diameter was 10 μm in a luminance-normalized stack. The expected fraction of image pixels belonging to nuclei was adjusted manually for each stack until the number of detected nuclei was reasonable, as judged by visual inspection. In most mice, GABAergic neurons were analyzed based on GCaMP6s fluorescence alone. Since fluorescence increases with neural activity, our sampling was biased toward active GABAergic neurons.

Laminar boundaries were defined as follows. The L1-L2 border was the depth at which pyramidal neurons first appeared. The L3-L4 border was defined as the point where a drop-off in labeled somata occurred. The L4-L5A border was defined as the point at which labeled somata reappeared. These boundaries were linearly adjusted to fit into the relative positioning defined by Hooks et al. (2011); the L2-L3 border was then extrapolated to occur at a defined relative position (13% of cortical depth) (Hooks et al., 2011).

Calcium Imaging Analysis

Imaging data were processed in five steps: intra-session registration, inter-session registration, ROI selection, ΔF/F calculation, and Ca^{2+} event extraction.

(1) Images were motion-corrected using an automated pipeline (Huber et al., 2012). First, registration was performed on individual behavioral trials: rigid registration was performed using a down-sampled fast Fourier transform (dFFT) (reference image, five consecutive frames of trial with minimal luminance change), followed by registration using a custom line-by-line algorithm (similar to Greenberg and Kerr, 2009). Second, registration was performed across trials within a session. The mean of a luminance-stable trial toward the middle of the session was employed as the reference image. All other trials were aligned to this trial using the dFFT, sometimes followed by a non-rigid interpolated warp field transform.

(2) Images were aligned across imaging sessions using the same interpolated warp field algorithm employed in the last step of inter-trial registration (Huber et al., 2012). The reference image for each session of a given imaging plane was registered to the reference images of other sessions. For all session pairs of a particular imaging plane, normalized cross-correlations were computed among the warp-field-registered reference images. The session with the highest median correlation to all other sessions was selected as the master reference image for that plane (typically, one of the middle imaging sessions). Manual inspection was used to exclude sessions whose reference image differed excessively from the master reference.

(3) ROIs were drawn using the master reference image from step 2 and then propagated to other imaging sessions using the warp-field transform. ROI drawing employed a custom user interface (MATLAB). A point near the cell center was selected. The algorithm constructed a matrix of intensities from the red channel (mCherry) where each column spanned a range of distances from the point and each row spanned all angles around the point. The sharpest intensity ridge along minimally varying distance was found, and this was treated as the border of the nucleus. The process was repeated, this time in the green channel (GCaMP) and starting with the nuclear border. This next ridge in angle-distance space was considered the outer border of the cytoplasm (Chen et al., 2013b). Pixels between these two ridges were assigned to the ROI. For L5 apical dendrite ROIs, the semi-automated algorithm looked for a single ridge in angle-distance space in the standard deviation image of the green channel (Figure S4). Pixels between the clicked location and the edge of the ridge were assigned to the ROI. For L4 axon imaging, ROIs consisted of a series of 12-by-12 μm squares on a 25 μm-spaced grid. For each ROI, a peri-somatic neuropil ROI was generated, consisting of an annulus 3 to 13 μm away from the outer edge of the ROI (Figure S3). Pixels with a correlation above 0.2 to an adjacent pixel as well as pixels belonging to non-neuropil ROIs were excluded from neuropil annuli.

(4) Raw fluorescence was extracted for each ROI, and fluorescence transients were neuropil-corrected ($F_{ROI\text{-}corrected} = F_{ROI} - \alpha F_{neuropil}$). If the corrected trace fell below a baseline ROI fluorescence, the value was set to baseline, so as to prevent over-correction. Neuropil correction used the local, peri-somatic neuropil signal, as using a global neuropil signal resulted in under-correction (Figure S3). The scaling factor, α, was set to 1, as manual inspection revealed that scaling factors below this produced under-correction. L4 axon imaging did not employ neuropil subtraction. F_0 was calculated using a 3 min sliding window. For cells with a highly skewed raw fluorescence distribution (generally, active neurons), the 5th percentile of raw fluorescence within the window was used as F_0; for cells with a symmetric distribution (generally, inactive neurons), the median was used. For cells with intermediate fluorescence distribution skewness, an intermediate percentile was used. $\Delta F/F = (F - F_0)/F_0$ was then calculated for each ROI.

(5) Event detection was performed using greedy template fitting of the ΔF/F trace (Figures 2G and 2H), which is similar to peeling approaches described previously (Lütcke et al., 2013). The template bank consisted of sums of exponentials with rise times of 3 to 5 frames (426 to 714 ms; see (Chen et al., 2013b)) and decay times of 7 to 35 frames (1 to 5 s). Candidate events were selected based on large second derivatives and convolved with the template bank. For each ROI, a noise estimate, σ, was obtained by subtracting a Savitzky-Golay fit of the trace and taking the standard deviation of the remaining trace. If any of the candidate events had a RMS difference of less than σ from the actual trace but were, on average, larger than σ in amplitude the event was accepted. That is, events had to be within the noise envelope of the actual trace, but had to have an amplitude exceeding noise. Accepted events were subtracted from the fluorescence trace, and the process repeated until no further events met the criteria.

We evaluated the performance of our event detector using simultaneous imaging and cell-attached recording data previously obtained in L2/3 of mouse visual cortex (Chen et al., 2013b). The data was degraded to match the per-neuron dwell time and sampling rate of the volume imaging employed in this study. For a false-positive detection rate of 0.01 Hz, 54% ± 10% of single action potentials (mean ± SD; n = 7 neurons) were detected.

Following event detection, a de-noised ΔF/F trace was produced by convolving events with appropriate amplitude, rise, and decay time constants. This trace was employed for all subsequent analyses, unless otherwise noted.

Model-Free Analysis of Task-Related Activity

Neurons were classified as task-related if their activity was distributed in a non-random manner relative to the structure of the trial. For each cell, we counted the fraction of trials during which a particular time bin had calcium events (Figures 4A and 4B). A null distribution was constructed by shuffling the calcium events in time for each ROI 10,000 times and performing the same analysis. For each shuffled iteration, the peak was determined (in units of fraction of trials with events). If the actual peak exceeded the 95th percentile of the shuffled peaks, the cell was scored as task related. This analysis was done separately for correct left and right trials; neurons satisfying the criteria on at least one of these two trial types were classified as task related.

Neurometric performance was measured for each neuron using ROC analysis. Individual trial responses were reduced to a decision variable based on the peri-stimulus time histogram (PSTH), as described previously (O'Connor et al., 2010b). Briefly, for all trials where the appropriate response was left or right (Figure 1A), a PSTH was computed using the event trace (event amplitude corresponded to ΔF/F amplitude, but no exponential decay was included). The dot product similarity of a trial's PSTH to the mean PSTH across respond-left trials minus the trial's dot product similarity to the respond-right PSTH was used as the decision variable. ROC analysis was performed using this decision variable, allowing us to determine how well an ideal observer could discriminate left from right trials. Both correct and incorrect trials were included. Trials in which the animal did not respond were excluded from the analysis. ROC analysis was performed on the real event trace as well as 100 traces with shuffled trial labels. Neurons with area under the curve (AUC) values exceeding the 95th percentile of shuffled AUCs were considered discriminative. Data were pooled across all volumetric sessions.

Population neurometric performance (Figure 6D) was assessed using a maximum likelihood decoder (naive Bayesian classifier), in which responses from different conditions were modeled as multivariate Gaussian distributions assuming zero covariance. The decoder was tasked with differentiating trials where the correct response was a left or a right lick; both hit and error trials were included. 5-fold cross-validation was employed, with each training set using 80% of trials and testing on the remaining 20%. Only neurons that were individually discriminative based on ROC analysis were included. One hundred groups of ten randomly selected discriminative neurons were tested for each day in each animal.

Model-Based Encoding Analysis

Neuronal encoding of behavioral variables was assessed by fitting a statistical model to every neuron independently. The model was a cascaded generalized linear model that predicted neuronal activity as a function of the whisker angle and curvature under a Gaussian noise model with input nonlinearities (Ahrens et al., 2008). Let s_1 be the time-varying whisker angle and let s_2 be the time-varying curvature. The model predicted the time-varying ΔF/F response r, as

$$r \sim Norm(z, \sigma^2)$$

$$z = f_1(s_1) * k_1 + f_2(s_2) * k_2,$$

where f_1 and f_2 are static, point-wise nonlinearities, and k_1 and k_2 are temporal kernels. k_1 and k_2 each consisted of 14 time points (2 s). f_1 and f_2 were each parameterized as a weighted sum of sixteen triangular "tent" basis functions:

$$f = \sum_{i=1}^{16} w_i b_i(x),$$

where x is the input (either s_1 or s_2), with each b_i given by

$$b_i = \begin{cases} (x - x_{i-1})/(x_i - x_{i-1}), & i > 1, x_{i-1} < x < x_i \\ (x_{i+1} - x)/(x_{i+1} - x_i), & i < N, x_i \le x < x_{i+1} \\ 0, \text{otherwise} \end{cases}.$$

Fitting of the model parameters k_1, k_2, f_1, and f_2 was performed using maximum likelihood with block coordinate descent. The model is bilinear in the parameters, and thus not globally convex, but it is convex when either the temporal kernels, or the nonlinearities, are held fixed (Ahrens et al., 2008). In these two cases, the remaining parameters can be estimated through convex optimization in closed form because of the Gaussian noise model (for other noise models it would require gradient descent). Thus, alternating coordinate descent on the full model can be performed (akin to alternating least-squares) (Young et al., 1976). Although not guaranteed to converge to a global minimum, this procedure was found to reliably estimate model parameters within approximately three to five iterations, achieving unique solutions both in simulation and in practice.

To remove degeneracy in the model associated with arbitrary scaling factors on either the kernels or the nonlinearities, the nonlinearities were forced to have minimum of 0 and maximum of 1. This constraint was applied after each iteration. No constraints were placed on the temporal kernels. In interpreting the results, however, the shape of the recovered nonlinearity is uninformative if the amplitude of the corresponding temporal kernel is near 0.

Whisker movements were sampled at 500 Hz while calcium responses were measured at 7 Hz. Given the nonlinearity in the model, additional information in the higher resolution whisker variables could be incorporated into the prediction. Specifically, the nonlinearity was applied to the whisker variables at their native temporal resolution, followed by linear down sampling to 7 Hz.

To prevent over-fitting, a prior was used to ensure smoothness of both the temporal kernels and the nonlinearities. Formally, this was implemented through a Gaussian prior on each set of parameters, with an inverse covariance given by the second derivative matrix (a matrix with values 2 and −1 for the main and off diagonals, respectively). Employing such a prior corresponds to maximizing the log-posterior, with the prior adding a small penalty to the objective function. In order to fit several thousand cells efficiently, the scale factor associated with this penalty was determined from a cross-validated inspection of a random subset of ROIs. On subsets of data, changing this parameter did not qualitatively change the fractions of neurons identified as touch or whisking.

Model fitting was performed using 5-fold cross-validation across trials (80% used for fitting, 20% used for model evaluation, with five distinct groupings per fit). Quality of fit was assessed using the Pearson correlation between the actual and model-predicted ΔF/F traces (R_{fit}; calculated on data not used for fitting). To assess the statistical significance of either the whisking or touch component of the response, a permutation test was employed. Specifically, the model was fit using only one of the two variables. In each case, the significance of that variable's contribution was assessed by repeating the fit using 100 time-shuffled ΔF/F traces. These were generated by taking the individual calcium events and distributing them randomly, while maintaining the rise and decay time constants associated with each event. If the actual model fit produced an R_{fit} in excess of the 95th percentile of shuffled R_{fit} values, the neuron was said to belong to that category. If both predictions were significant, the neuron was considered as belonging to both categories. The 95th percentile criterion was employed throughout, unless otherwise noted.

For imaging during learning, the encoding model was fit to data from individual sessions using a more stringent 99th percentile criterion. On days where multiple whiskers were present, only the eventual spared whisker's curvature and angle information were employed for encoding model fitting. For trend analysis during learning, two sessions per animal were employed to increase statistical power (Figures 6C–6E).

For volumetric imaging and L4 axon imaging, the model was fit to data pooled across all sessions for which a given ROI was imaged. Volume maps (Figures 7 and S5) were constructed by pooling data across all relevant animals and collapsing from four quadrants into one in arc-row space. Maps were constructed with a more stringent inclusion criterion: only cells with R_{fit} > 99th percentile of event-shuffled R_{fit}s were included. Voxels for arc-depth and row-depth were 15 μm by 15 μm by a half-barrel width in size, and the fraction was estimated for a voxel using pooled data. Arc-row voxels were 15 by 15 μm, spanning all depths, but restricted to specified cell types.

The encoding model-derived static nonlinearity for curvature in touch neurons was equivalent to a receptive field, with whisker-curvature-dependent amplitude ranging from 0 to 1 (Figures 5C, 5D, and 8B). Because curvature is proportional to the force experienced by the whisker follicle (Birdwell et al., 2007; Pammer et al., 2013), and because most whisker motion is along a single plane, the sign of the curvature change provided directional tuning. Negative curvature changes correspond to pole contacts during protraction, whereas positive curvature changes correspond to contacts during retraction.

We derived a DI that was negative for neurons preferring retraction touch and positive for neurons preferring protraction touch (Figure 8B, inset). The index, DI, was simply the ratio of the difference between the amplitude of the force kernel at the maximal protraction and retraction $\Delta\kappa$ value divided by the sum.

Directionality maps were constructed for cells with R_{fit} values above the 99th percentile of event-shuffled R_{fit}s (Figure 8D). The map consisted of 50 μm by 50 μm voxels spanning depth (300 μm). The stability of directional preference was assessed using the average pairwise RMS of the curvature static nonlinearities for touch neurons (Figure S7). To restrict the data set to neurons responding to mainly touch-induced curvature changes, the 99th percentile criterion was employed and the touch R_{fit} had to exceed 0.25.

In anesthetized mice, direction tuning was measured for ROIs showing a significant response to piezo deflection, defined as a trial-locked mean response whose amplitude exceeded the 95th percentile of an event-shuffled null distribution. ROIs were further required to have event rates above 0.01 Hz. The DI for ROIs meeting this criterion was defined as the difference between the peak ΔF/F response to rearward (R) and forward (F) deflection divided by their sum: $DI_{anesthetized} = (R - F)/(R + F)$.

Publicly Available Data set

The imaging data (Table S1) are publicly available at http://dx.doi.org/10.6080/K0TB14TN. This includes the raw and processed calcium imaging data, raw and processed whisker videography, and behavioral data.

SUPPLEMENTAL INFORMATION

Supplemental Information includes seven figures, one table, and Supplemental Experimental Procedures and can be found with this article online at http://dx.doi.org/10.1016/j.neuron.2015.03.027.

ACKNOWLEDGMENTS

We thank Diego Gutnisky, Nuo Li, Nick Sofroniew, and Jianing Yu for comments on the manuscript and discussion; Amy Hu for histology; and Fernando Amat for the Gaussian mixture model code. The Janelia GENIE project provided reagents before publication. This work was funded by the Howard Hughes Medical Institute.

Received: November 1, 2014
Revised: January 29, 2015
Accepted: March 11, 2015
Published: April 23, 2015

REFERENCES

Ahissar, E., Sosnik, R., Bagdasarian, K., and Haidarliu, S. (2001). Temporal frequency of whisker movement. II. Laminar organization of cortical representations. J. Neurophysiol. *86*, 354–367.

Ahrens, M.B., Paninski, L., and Sahani, M. (2008). Inferring input nonlinearities in neural encoding models. Network *19*, 35–67.

Andermann, M.L., and Moore, C.I. (2006). A somatotopic map of vibrissa motion direction within a barrel column. Nat. Neurosci. *9*, 543–551.

Andermann, M.L., Kerlin, A.M., and Reid, R.C. (2010). Chronic cellular imaging of mouse visual cortex during operant behavior and passive viewing. Front. Cell Neurosci. *4*, 3.

Armstrong-James, M., Fox, K., and Das-Gupta, A. (1992). Flow of excitation within rat barrel cortex on striking a single vibrissa. J. Neurophysiol. *68*, 1345–1358.

Barth, A.L., and Poulet, J.F. (2012). Experimental evidence for sparse firing in the neocortex. Trends Neurosci. *35*, 345–355.

Birdwell, J.A., Solomon, J.H., Thajchayapong, M., Taylor, M.A., Cheely, M., Towal, R.B., Conradt, J., and Hartmann, M.J. (2007). Biomechanical models for radial distance determination by the rat vibrissal system. J. Neurophysiol. *98*, 2439–2455.

Chen, J.L., Carta, S., Soldado-Magraner, J., Schneider, B.L., and Helmchen, F. (2013a). Behaviour-dependent recruitment of long-range projection neurons in somatosensory cortex. Nature *499*, 336–340.

Chen, T.W., Wardill, T.J., Sun, Y., Pulver, S.R., Renninger, S.L., Baohan, A., Schreiter, E.R., Kerr, R.A., Orger, M.B., Jayaraman, V., et al. (2013b). Ultrasensitive fluorescent proteins for imaging neuronal activity. Nature *499*, 295–300.

Clack, N.G., O'Connor, D.H., Huber, D., Petreanu, L., Hires, A., Peron, S., Svoboda, K., and Myers, E.W. (2012). Automated tracking of whiskers in videos of head fixed rodents. PLoS Comput. Biol. *8*, e1002591.

Crochet, S., Poulet, J.F., Kremer, Y., and Petersen, C.C. (2011). Synaptic mechanisms underlying sparse coding of active touch. Neuron *69*, 1160–1175.

Curtis, J.C., and Kleinfeld, D. (2009). Phase-to-rate transformations encode touch in cortical neurons of a scanning sensorimotor system. Nat. Neurosci. *12*, 492–501.

de Kock, C.P., and Sakmann, B. (2009). Spiking in primary somatosensory cortex during natural whisking in awake head-restrained rats is cell-type specific. Proc. Natl. Acad. Sci. USA *106*, 16446–16450.

Denk, W., Delaney, K.R., Gelperin, A., Kleinfeld, D., Strowbridge, B.W., Tank, D.W., and Yuste, R. (1994). Anatomical and functional imaging of neurons using 2-photon laser scanning microscopy. J. Neurosci. Methods *54*, 151–162.

Derdikman, D., Hildesheim, R., Ahissar, E., Arieli, A., and Grinvald, A. (2003). Imaging spatiotemporal dynamics of surround inhibition in the barrels somatosensory cortex. J. Neurosci. *23*, 3100–3105.

Diamond, M.E., von Heimendahl, M., Knutsen, P.M., Kleinfeld, D., and Ahissar, E. (2008). 'Where' and 'what' in the whisker sensorimotor system. Nat. Rev. Neurosci. *9*, 601–612.

Dombeck, D.A., Khabbaz, A.N., Collman, F., Adelman, T.L., and Tank, D.W. (2007). Imaging large-scale neural activity with cellular resolution in awake, mobile mice. Neuron *56*, 43–57.

Fan, G.Y., Fujisaki, H., Miyawaki, A., Tsay, R.K., Tsien, R.Y., and Ellisman, M.H. (1999). Video-rate scanning two-photon excitation fluorescence microscopy and ratio imaging with cameleons. Biophys. J. *76*, 2412–2420.

Fee, M.S., Mitra, P.P., and Kleinfeld, D. (1997). Central versus peripheral determinants of patterned spike activity in rat vibrissa cortex during whisking. J. Neurophysiol. *78*, 1144–1149.

Feldmeyer, D. (2012). Excitatory neuronal connectivity in the barrel cortex. Front. Neuroanat. *6*, http://dx.doi.org/10.3389/fnana.2012.00024.

Feldmeyer, D., Brecht, M., Helmchen, F., Petersen, C.C., Poulet, J.F., Staiger, J.F., Luhmann, H.J., and Schwarz, C. (2013). Barrel cortex function. Prog. Neurobiol. *103*, 3–27.

Gorski, J.A., Talley, T., Qiu, M., Puelles, L., Rubenstein, J.L., and Jones, K.R. (2002). Cortical excitatory neurons and glia, but not GABAergic neurons, are produced in the Emx1-expressing lineage. J. Neurosci. *22*, 6309–6314.

Greenberg, D.S., and Kerr, J.N. (2009). Automated correction of fast motion artifacts for two-photon imaging of awake animals. J. Neurosci. Methods *176*, 1–15.

Guo, Z.V., Hires, S.A., Li, N., O'Connor, D.H., Komiyama, T., Ophir, E., Huber, D., Bonardi, C., Morandell, K., Gutnisky, D., et al. (2014a). Procedures for behavioral experiments in head-fixed mice. PLoS ONE *9*, e88678.

Guo, Z.V., Li, N., Huber, D., Ophir, E., Gutnisky, D.A., Ting, J.T., Feng, G., and Svoboda, K. (2014b). Flow of cortical activity underlying a tactile decision in mice. Neuron *81*, 179–194.

Helmchen, F., Svoboda, K., Denk, W., and Tank, D.W. (1999). In vivo dendritic calcium dynamics in deep-layer cortical pyramidal neurons. Nat. Neurosci. *2*, 989–996.

Hill, D.N., Varga, Z., Jia, H., Sakmann, B., and Konnerth, A. (2013). Multibranch activity in basal and tuft dendrites during firing of layer 5 cortical neurons in vivo. Proc. Natl. Acad. Sci. USA *110*, 13618–13623.

Hires, S.A., Pammer, L., Svoboda, K., and Golomb, D. (2013). Tapered whiskers are required for active tactile sensation. eLife *2*, e01350.

Holekamp, T.F., Turaga, D., and Holy, T.E. (2008). Fast three-dimensional fluorescence imaging of activity in neural populations by objective-coupled planar illumination microscopy. Neuron *57*, 661–672.

Hooks, B.M., Hires, S.A., Zhang, Y.X., Huber, D., Petreanu, L., Svoboda, K., and Shepherd, G.M. (2011). Laminar analysis of excitatory local circuits in vibrissal motor and sensory cortical areas. PLoS Biol. *9*, e1000572.

Huber, D., Gutnisky, D.A., Peron, S., O'Connor, D.H., Wiegert, J.S., Tian, L., Oertner, T.G., Looger, L.L., and Svoboda, K. (2012). Multiple dynamic representations in the motor cortex during sensorimotor learning. Nature *484*, 473–478.

Hutson, K.A., and Masterton, R.B. (1986). The sensory contribution of a single vibrissa's cortical barrel. J. Neurophysiol. *56*, 1196–1223.

Jadhav, S.P., Wolfe, J., and Feldman, D.E. (2009). Sparse temporal coding of elementary tactile features during active whisker sensation. Nat. Neurosci. *12*, 792–800.

Ji, N., Sato, T.R., and Betzig, E. (2012). Characterization and adaptive optical correction of aberrations during in vivo imaging in the mouse cortex. Proc. Natl. Acad. Sci. USA *109*, 22–27.

Kerlin, A.M., Andermann, M.L., Berezovskii, V.K., and Reid, R.C. (2010). Broadly tuned response properties of diverse inhibitory neuron subtypes in mouse visual cortex. Neuron *67*, 858–871.

Kerr, J.N., Greenberg, D., and Helmchen, F. (2005). Imaging input and output of neocortical networks in vivo. Proc. Natl. Acad. Sci. USA *102*, 14063–14068.

Kerr, J.N., de Kock, C.P., Greenberg, D.S., Bruno, R.M., Sakmann, B., and Helmchen, F. (2007). Spatial organization of neuronal population responses in layer 2/3 of rat barrel cortex. J. Neurosci. *27*, 13316–13328.

Kinnischtzke, A.K., Simons, D.J., and Fanselow, E.E. (2014). Motor cortex broadly engages excitatory and inhibitory neurons in somatosensory barrel cortex. Cereb. Cortex *24*, 2237–2248.

Knutsen, P.M., Pietr, M., and Ahissar, E. (2006). Haptic object localization in the vibrissal system: behavior and performance. J. Neurosci. *26*, 8451–8464.

Knutsen, P.M., Biess, A., and Ahissar, E. (2008). Vibrissal kinematics in 3D: tight coupling of azimuth, elevation, and torsion across different whisking modes. Neuron *59*, 35–42.

Komiyama, T., Sato, T.R., O'Connor, D.H., Zhang, Y.X., Huber, D., Hooks, B.M., Gabitto, M., and Svoboda, K. (2010). Learning-related fine-scale specificity imaged in motor cortex circuits of behaving mice. Nature *464*, 1182–1186.

Kremer, Y., Léger, J.F., Goodman, D., Brette, R., and Bourdieu, L. (2011). Late emergence of the vibrissa direction selectivity map in the rat barrel cortex. J. Neurosci. *31*, 10689–10700.

Krupa, D.J., Wiest, M.C., Shuler, M.G., Laubach, M., and Nicolelis, M.A. (2004). Layer-specific somatosensory cortical activation during active tactile discrimination. Science *304*, 1989–1992.

Lefort, S., Tomm, C., Floyd Sarria, J.C., and Petersen, C.C. (2009). The excitatory neuronal network of the C2 barrel column in mouse primary somatosensory cortex. Neuron *61*, 301–316.

Lu, S.M., and Lin, R.C.S. (1993). Thalamic afferents of the rat barrel cortex: a light- and electron-microscopic study using *Phaseolus vulgaris* leucoagglutinin as an anterograde tracer. Somatosens. Mot. Res. *10*, 1–16.

Lütcke, H., Gerhard, F., Zenke, F., Gerstner, W., and Helmchen, F. (2013). Inference of neuronal network spike dynamics and topology from calcium imaging data. Front. Neural Circuits *7*, 201.

Madisen, L., Mao, T., Koch, H., Zhuo, J.M., Berenyi, A., Fujisawa, S., Hsu, Y.W., Garcia, A.J., 3rd, Gu, X., Zanella, S., et al. (2012). A toolbox of Cre-dependent optogenetic transgenic mice for light-induced activation and silencing. Nat. Neurosci. *15*, 793–802.

Margolis, D.J., Lütcke, H., Schulz, K., Haiss, F., Weber, B., Kügler, S., Hasan, M.T., and Helmchen, F. (2012). Reorganization of cortical population activity imaged throughout long-term sensory deprivation. Nat. Neurosci. *15*, 1539–1546.

Masamizu, Y., Tanaka, Y.R., Tanaka, Y.H., Hira, R., Ohkubo, F., Kitamura, K., Isomura, Y., Okada, T., and Matsuzaki, M. (2014). Two distinct layer-specific dynamics of cortical ensembles during learning of a motor task. Nat. Neurosci. *17*, 987–994.

Miri, A., Daie, K., Burdine, R.D., Aksay, E., and Tank, D.W. (2011). Regression-based identification of behavior-encoding neurons during large-scale optical imaging of neural activity at cellular resolution. J. Neurophysiol. *105*, 964–980.

Nagai, T., Yamada, S., Tominaga, T., Ichikawa, M., and Miyawaki, A. (2004). Expanded dynamic range of fluorescent indicators for Ca(2+) by circularly permuted yellow fluorescent proteins. Proc. Natl. Acad. Sci. USA *101*, 10554–10559.

O'Connor, D.H., Clack, N.G., Huber, D., Komiyama, T., Myers, E.W., and Svoboda, K. (2010a). Vibrissa-based object localization in head-fixed mice. J. Neurosci. *30*, 1947–1967.

O'Connor, D.H., Peron, S.P., Huber, D., and Svoboda, K. (2010b). Neural activity in barrel cortex underlying vibrissa-based object localization in mice. Neuron *67*, 1048–1061.

O'Connor, D.H., Hires, S.A., Guo, Z.V., Li, N., Yu, J., Sun, Q.Q., Huber, D., and Svoboda, K. (2013). Neural coding during active somatosensation revealed using illusory touch. Nat. Neurosci. *16*, 958–965.

Ohki, K., Chung, S., Kara, P., Hübener, M., Bonhoeffer, T., and Reid, R.C. (2006). Highly ordered arrangement of single neurons in orientation pinwheels. Nature *442*, 925–928.

Ohtsuki, G., Nishiyama, M., Yoshida, T., Murakami, T., Histed, M., Lois, C., and Ohki, K. (2012). Similarity of visual selectivity among clonally related neurons in visual cortex. Neuron *75*, 65–72.

Pammer, L., O'Connor, D.H., Hires, S.A., Clack, N.G., Huber, D., Myers, E.W., and Svoboda, K. (2013). The mechanical variables underlying object localization along the axis of the whisker. J. Neurosci. *33*, 6726–6741.

Paninski, L., Pillow, J.W., and Simoncelli, E.P. (2004). Maximum likelihood estimation of a stochastic integrate-and-fire neural encoding model. Neural Comput. *16*, 2533–2561.

Peters, A.J., Chen, S.X., and Komiyama, T. (2014). Emergence of reproducible spatiotemporal activity during motor learning. Nature *510*, 263–267.

Petersen, C.C., and Crochet, S. (2013). Synaptic computation and sensory processing in neocortical layer 2/3. Neuron *78*, 28–48.

Petreanu, L., Mao, T., Sternson, S.M., and Svoboda, K. (2009). The subcellular organization of neocortical excitatory connections. Nature *457*, 1142–1145.

Pillow, J.W., Shlens, J., Paninski, L., Sher, A., Litke, A.M., Chichilnisky, E.J., and Simoncelli, E.P. (2008). Spatio-temporal correlations and visual signalling in a complete neuronal population. Nature *454*, 995–999.

Polley, D.B., Kvasnák, E., and Frostig, R.D. (2004). Naturalistic experience transforms sensory maps in the adult cortex of caged animals. Nature *429*, 67–71.

Pologruto, T.A., Sabatini, B.L., and Svoboda, K. (2003). ScanImage: flexible software for operating laser scanning microscopes. Biomed. Eng. Online *2*, 13.

Prevedel, R., Yoon, Y.G., Hoffmann, M., Pak, N., Wetzstein, G., Kato, S., Schrödel, T., Raskar, R., Zimmer, M., Boyden, E.S., and Vaziri, A. (2014). Simultaneous whole-animal 3D imaging of neuronal activity using light-field microscopy. Nat. Methods *11*, 727–730.

Quist, B.W., and Hartmann, M.J. (2012). Mechanical signals at the base of a rat vibrissa: the effect of intrinsic vibrissa curvature and implications for tactile exploration. J. Neurophysiol. *107*, 2298–2312.

Romo, R. (2013). Conversion of sensory signals into perceptions, memories and decisions. Prog. Neurobiol. *103*, 1–2.

Sato, T.R., and Svoboda, K. (2010). The functional properties of barrel cortex neurons projecting to the primary motor cortex. J. Neurosci. *30*, 4256–4260.

Sato, T.R., Gray, N.W., Mainen, Z.F., and Svoboda, K. (2007). The functional microarchitecture of the mouse barrel cortex. PLoS Biol. *5*, e189.

Shaner, N.C., Campbell, R.E., Steinbach, P.A., Giepmans, B.N., Palmer, A.E., and Tsien, R.Y. (2004). Improved monomeric red, orange and yellow fluorescent proteins derived from Discosoma sp. red fluorescent protein. Nat. Biotechnol. *22*, 1567–1572.

Shih, A.Y., Blinder, P., Tsai, P.S., Friedman, B., Stanley, G., Lyden, P.D., and Kleinfeld, D. (2013). The smallest stroke: occlusion of one penetrating vessel leads to infarction and a cognitive deficit. Nat. Neurosci. *16*, 55–63.

Simons, D.J. (1978). Response properties of vibrissa units in rat SI somatosensory neocortex. J. Neurophysiol. *41*, 798–820.

Sofroniew, N.J., Cohen, J.D., Lee, A.K., and Svoboda, K. (2014). Natural whisker-guided behavior by head-fixed mice in tactile virtual reality. J. Neurosci. *34*, 9537–9550.

Staiger, J.F., Bojak, I., Miceli, S., and Schubert, D. (2014). A gradual depth-dependent change in connectivity features of supragranular pyramidal cells in rat barrel cortex. Brain Struct. Funct. Published online February 26, 2014.

Stevenson, I.H., and Kording, K.P. (2011). How advances in neural recording affect data analysis. Nat. Neurosci. *14*, 139–142.

Stosiek, C., Garaschuk, O., Holthoff, K., and Konnerth, A. (2003). In vivo two-photon calcium imaging of neuronal networks. Proc. Natl. Acad. Sci. USA *100*, 7319–7324.

Svoboda, K., and Yasuda, R. (2006). Principles of two-photon excitation microscopy and its applications to neuroscience. Neuron *50*, 823–839.

Svoboda, K., Denk, W., Kleinfeld, D., and Tank, D.W. (1997). In vivo dendritic calcium dynamics in neocortical pyramidal neurons. Nature *385*, 161–165.

Svoboda, K., Helmchen, F., Denk, W., and Tank, D.W. (1999). Spread of dendritic excitation in layer 2/3 pyramidal neurons in rat barrel cortex in vivo. Nat. Neurosci. *2*, 65–73.

Tian, L., Hires, S.A., Mao, T., Huber, D., Chiappe, M.E., Chalasani, S.H., Petreanu, L., Akerboom, J., McKinney, S.A., Schreiter, E.R., et al. (2009). Imaging neural activity in worms, flies and mice with improved GCaMP calcium indicators. Nat. Methods *6*, 875–881.

Timofeeva, E., Mérette, C., Emond, C., Lavallée, P., and Deschênes, M. (2003). A map of angular tuning preference in thalamic barreloids. J. Neurosci. *23*, 10717–10723.

Trachtenberg, J.T., Chen, B.E., Knott, G.W., Feng, G., Sanes, J.R., Welker, E., and Svoboda, K. (2002). Long-term in vivo imaging of experience-dependent synaptic plasticity in adult cortex. Nature *420*, 788–794.

von Heimendahl, M., Itskov, P.M., Arabzadeh, E., and Diamond, M.E. (2007). Neuronal activity in rat barrel cortex underlying texture discrimination. PLoS Biol. *5*, e305.

Wimmer, V.C., Bruno, R.M., de Kock, C.P., Kuner, T., and Sakmann, B. (2010). Dimensions of a projection column and architecture of VPM and POm axons in rat vibrissal cortex. Cereb. Cortex *20*, 2265–2276.

Woolsey, T.A., and Van der Loos, H. (1970). The structural organization of layer IV in the somatosensory region (SI) of mouse cerebral cortex. The description of a cortical field composed of discrete cytoarchitectonic units. Brain Res. *17*, 205–242.

Young, F.W., Deleeuw, J., and Takane, Y. (1976). Regression with Qualitative and Quantitative Variables - Alternating Least-Squares Method with Optimal Scaling Features. Psychometrika *41*, 505–529.